University of Wisconsin Milwaukee

UWM Digital Commons

May 2023

Numerical Simulations of Tidal Disruption Events

Alexandra Elise Spaulding
University of Wisconsin-Milwaukee

Recommended Citation

NUMERICAL SIMULATIONS OF TIDAL DISRUPTION EVENTS

by

Alexandra Spaulding

A Dissertation Submitted in

Partial Fulfillment of the

Requirements for the Degree of

Doctor of Philosophy

in Physics

at

The University of Wisconsin-Milwaukee

May 2023

ABSTRACT

NUMERICAL SIMULATIONS OF TIDAL DISRUPTION EVENTS

by

Alexandra Spaulding

The University of Wisconsin-Milwaukee, 2023
Under the Supervision of Professor Philip Chang, PhD

The detection of supermassive black holes (SMBH) in our universe has proven to be a challenge. One way to find an SMBH in a quiescent, inactive galaxy is through a tidal disruption event, or a TDE. A TDE occurs when a star is slightly perturbed and is subsequently disrupted by the SMBH. When this happens, part of the debris from the disrupted star remains bound to the SMBH while the rest is unbound. The SMBH accretes the bound matter and reveals their presence by a temporary X-ray flare, lasting a few months. Using conservation of energy, the fallback rate of the material to the SMBH can be shown to follow a timescale of $t^{-5/3}$. However, the complete picture of TDEs is not well understood due to the diverse physics involved, and therefore TDEs necessitates 3-D numerical simulations to dive deeper into the physics that are at play in a TDE. Here two methodologies are commonly employed, each of which comes with its own set of advantages: smoothed-particle hydrodynamics and Eulerian grid codes. A hybrid of these methods known as the moving-mesh code has been developed in an attempt to capture the best characteristics of each. We use the moving-mesh solver MANGA to study characteristics of TDEs.

In this work, we begin with an introduction to TDEs in Chapter 1. We describe their observational characteristics, the mechanics of the event and the dynamics of the disruption. Next, we present two different simulation techniques in Chapter 2 and how the best

aspects of each are combined in the technique used for our work, moving-mesh. In Chapter 3, we introduce a parameter study of the effect of impact parameter on the energy distribution of the debris. We show how this influences the fallback rate of the unbound debris, the time of peak accretion and the evolution of the accretion rate. In Chapter 4 we further investigate how this result determines the expected radio emission from the TDE. With observed radio emission from TDEs, we show that it is possible to determine the density profile of the surrounding medium.

TDE simulations to date mostly ignore the influence of an initial magnetic field on the surface of the star. In Chapter 5 we describe a recently implemented magnetohydrodynamics scheme in MANGA. When we apply an initial magnetic field to the star, we notice an outflow from the TDE that is not present in our simulations without an initial magnetic field. We model the outflow as an expanding photosphere and relate our results to observational signatures of several TDEs.

TABLE OF CONTENTS

LIST OF FIGURES

LIST OF TABLES

LIST OF ABBREVIATIONS

AGN . .   active galactic nuclei

ALE . .   arbitrary Lagrangian-Eulerian

AMR . .   adaptive mesh refinement

ASAS-SN   All Sky Automated Survey for supernovae

ATLAS .   Asteriod Terrestrial-impact Last Alert System

BH . . .   black hole

ChaNGa   Charm N-body GrAvity solver

CM . .   center of mass

CNSS .   Caltech–NRAO Stripe 82 Survey

CT . . .   constrained transport

EOS . .   equation of state

GALEX   Galaxy Evolution Explorer

GR . . .   general relativity

GRHD .   general relativistic hydrodynamics

ISM . .   interstellar medium

LSST . .   Legacy Survey of Space and Time

$M_\odot$ . . .   solar mass

MANGA   moving-mesh ChaNGa

MESA .   Modules for Experiments in Stellar Astrophysics

MHD .   magnetohydrodynamics

MM . .   moving-mesh

OGLE .   Optical Gravitational Lensing Experiment

PTF .. Palomar Transient Factory

$R_\odot$ ... solar radius

RHD .. radiation hydrodynamics

SDSS .. Sloan Digital Sky Survey

SMBH . supermassive black hole

SN ... supernovae

SPH .. smoothed-particle hydrodynamics

TDE .. tidal disruption events

UV ... ultraviolet

VLA .. very large array

ZAMS . zero-age main sequence

ZTF .. Zwicky Transient Facility

ACKNOWLEDGMENTS

CHAPTER 1

Introduction to Tidal Disruption Events

1.1 SMBHS IN OUR UNIVERSE

The detection of supermassive black holes (SMBH) in our universe has proven to be a challenge. Today, it is accepted that a SMBH lies at the nuclei of all massive galaxies (Ferrarese & Ford, 2005). Scientists struggled to identify these SMBH because while 10% of galaxies were Active Galactic Nuclei (AGN) and believed to be powered by accretion onto supermassive black holes (SMBH), the remaining 90% were quiescent, inactive galaxies with no signs of permanent activity. Only in a handful of the closest (quiescent) galaxies, could SMBHs be discerned by their impact on stellar rotation curves (Sargent et al., 1978). In order to tell whether SMBHs existed not only in AGN, but in the majority of quiescent galaxies, Rees (1988) suggested that, if an unlucky star got sufficiently close to an SMBH, it would be disrupted. Subsequently, the SMBH would accrete the matter and would reveal their presence by a temporary X-ray flare, lasting a few months. When this happens, we call these tidal disruption events, or TDEs. In this thesis, we begin with the history of SMBH research, and aim to demonstrate how TDEs are an essential tool in understanding SMBHs, accretion physics, jet propulsion and more.

1.1.1 Motivation

Black holes are laboratories for testing fundamental theories that explain how the universe works on the largest and smallest scales. There is ample indirect evidence from various astronomical studies indicating that black holes exist, including the investigation of nearby objects that are subjected to the gravitational pull of a black hole. These are circumstances well explained by the General Theory of Relativity (GR), the large scale.

On the small scale, quantum physics can be studied by looking at the Hawking radiation that leaves a black hole. While each of these theories works well in its respective regime, physicists currently do not understand how to create a single physical theory that would be universal and, hence, explain the physics of black holes in detail.

In addition to the fundamental physical theories, there are many details of plasma physics that are not completely understood. Properties of the hot gas surrounding and being pulled into the black hole beyond the event horizon are not fully known.

1.1.2 Methods for finding SMBH

Energetic emission from accretion disks around young SMBHs are one way these objects can be detected. These quasars give us information about only a small fraction of SMBHs which are accreting gas at a high rate. Our universe is believed to be comprised of a larger population of non-accreting SMBHs that cannot be detected by emission from actively accreting gas. An alternative way to detect SMBHs such as these is to study the motion of the stars around it. This method gives us information about the center of nearby galaxies, but is limited by the resolution of our telescopes. For example, one way to determine the mass of an object in the center of a galaxy, or a BH, is by looking at stellar orbits around the BH. Ghez et al. (2005) used the W. M. Keck I 10m telescope to calculate the mass of our galaxy's central BH with the orbits of the stars they observed and found $M_{BH} = 3.7(\pm 0.2) \times 10^6 [R_0/(8 \text{ kpc})]^3 M_\odot$. Genzel et al. (2010) also used stars' orbits to find a mass of $4.4 \pm 0.3 \times 10^6 M_\odot$ in the center of our galaxy. Gebhardt et al. (2011) and Kormendy et al. (2009) look at stellar dispersion in a galaxy to determine the mass of the central black hole using a $M_{BH} - \sigma$ relationship, where σ is the velocity dispersion. A method to study SMBHs of farther galaxies is looking at stellar disruptions. If a star passes too close to a SMBH, the tidal forces from the SMBH can overcome the self gravity forces of the star

and result in partial or complete disruption of the star. Some of the material from the disrupted star remains bound to the SMBH and creates a highly luminous accretion disk that can be detected. These events are called tidal disruption events (TDEs) and can be an extremely informative way to give us insights on SMBHs in the center of quiescent galaxies.

1.2 OBSERVATIONS OF TIDAL DISRUPTION EVENTS

Tidal disruption events are a relatively new field of study, and 100 have been detected since 1990. The first TDEs were found by X-ray instruments, however TDEs peak in the optical and UV wavelength. Since the mid-1990s, detections have increased rapidly with the quality of instruments increasing. Multi-wavelength observations of TDEs will be key to distinguish them from other high energy emission astrophysical events.

1.2.1 X-ray

Observational astronomy of tidal disruption events began with the detection of X-ray flares from quiescent galaxies during the ROSAT all-sky survey of 1990-1991 (Saxton et al., 2020). During the TDE process, roughly half of the stellar material is accreted onto the SMBH, resulting in a flare of radiation peaking in soft X-ray and UV band, fading away on timescales of months to years (Rees, 1988). The X-rays generated during a TDE are believed to be produced from the innermost stable orbits of the black hole and experience the strong gravitational field. The observed X-ray light curves of TDEs typically follow a power-law decline approximately by $t^{-5/3}$ over timescales of months to years, roughly consistent with the theoretical prediction (e.g. Rees (1988), see also Section 1.3). Their luminosity peaks around 4 $\times 10^{44}$ erg/s (near-Eddington) and have a thermal spectrum with $kT \approx$ few $\times 10^5$ K. X-ray luminosity from TDEs can show variability of more than a

couple orders of magnitude within a couple years, while standard AGN vary their X-ray luminosity by factors of a few (Li et al., 2020). X-ray emission of a TDE is a key component of locating a quiescent SMBH because it is orders of magnitude higher than luminosity of other X-ray transient phenomena such as Supernovae, accreting galactic binaries, and flare stars (Li et al., 2020).

The first detections of TDE X-ray flares were made with the ROSAT satellite, which found transient sources that displayed the predicted TDE characteristics; a short rise to peak, a steady decline, high peak luminosities, a soft X-ray spectrum, and, importantly, occurred in quiescent, in-active galaxies. As instruments such as Chandra, XMM-Newton and Swift have been introduced, the X-ray spectra of TDEs has become more understood and more distinguishable from AGN (Esquej et al., 2007; Lin et al., 2011; Saxton et al., 2012). At the time of this writing, more than 20 TDEs have been detected in X-ray's.

1.2.2 Radio

A small fraction of TDEs (at most a few percent) have been observed to produce radio-luminous mildly relativistic jets. The remainder of the population are radio quiet, producing less luminous jets, non-relativistic outflows or, possibly, no radio emission at all. Radio observations contribute to our understanding of TDEs because they can provide key diagnostics such as calorimetry, outflow velocity, magnetic field strength, and the density of the immediate environments surrounding the transient. Current radio observations of TDEs have revealed extremely diverse radio properties, such as a range in luminosity of 10^{36} to 10^{42} erg/s (Alexander et al., 2020).

The physical mechanism used to produce radio emission in TDEs is not entirely clear. The basic mechanism believed to be responsible for radio emission in all types of transients, including TDEs, is synchrotron emission. Synchrotron emission occurs when a

fast outflow interacts with the interstellar medium. As the shockwave moves through the ISM, it accelerates free electrons to relativistic velocities and increases the magnitude of magnetic fields. The physical properties of the system such as velocity of the outflow, density of the medium, the total energy carried by the outflow and more shape the properties of the observed synchrotron emission. Because of this, radio emission from TDEs can give us a great range of information about the system.

To date, around 9 TDEs have published radio detections references. TDEs with radio emission have been detected using followup observations with the Karl G. Jansky Very Large Array (VLA) (Alexander et al., 2016). However, to date there is only one TDE that was first detected in the radio, CNSS J001947.3+003527. CNSS J001947.3+003527 was detected with the Caltech–NRAO Stripe 82 Survey (CNSS), a dedicated radio transient survey carried out with the VLA.

The range in radio luminosity described previously is thought to be attributed to the fact that high luminosity TDEs launch very energetic relativistic jets view on-axis, while the lower luminosity or "radio-quiet" TDEs either launch jets off axis or do not launch jets at all. However, other factors such as ISM density, magnetic field strength, and distribution geometry may also contribute to the wide range in observed radio luminosity (Krolik et al., 2016; Yalinewich et al., 2019a).

Two TDEs that have been detected in the radio and well studied are Sw J1644+57 and ASASSN-14li (mentioned also in Section 1.2.3). Sw J1644+57 was discovered by the Neils Gehrels Swift Observatory at z = 0.354. It was first discovered in the X-ray, and associated radio emission was discovered within 24 hours. This emission is consistent with synchrotron emission from a an initially mildly relativistic jet that expands and slowly decelerates (Zauderer et al., 2011, 2013; Berger et al., 2012). ASASSN-14li was detected at z = 0.0206, much closer than Sw J1644+57. As mentioned, it was first detected in the

optical/UV and subsequently detected across the electromagnetic spectrum.

ASASSN-14li had a radio luminosity 10^3 times less than Sw J1644+57. There are several different models that have been proposed to explain its radio emission. The first of these is that it arises from a non-relativistic wind (Alexander et al., 2016). Alexander et al. (2016) modeled the radio emission as synchrotron emission arising from the external shock between outflowing material from the TDE and the surrounding circumnuclear medium. A second proposed method for synchrotron emission is from the unbound tidal debris stream, which we explore in Section 4.2. In this method, half of the disrupted star is unbound and as it travels through space, it will interact with the ISM, creating a bow shock. Only a small fraction of material in the unbound debris is required to produce thee observed radio luminosity. Krolik et al. (2016) performed an equipartition analysis according to this model and found similar velocities and energies of the radio-emitting material as Alexander et al. (2016). We go more into depth on this model in Section 4.2.

A third proposed model for the radio emission of ASSASN-14li is emission from a sub-relativistic jet. In this model, emission comes either from interaction with the surrounding medium, or internal shocks inside the jets (Alexander et al., 2016). The external mode of emission is akin to the wind and unbound-debris models discussed above where the jet drives into the surrounding medium, creating a forward shock. The internal shock model is argued for with evidence of a link between the X-ray and radio light curves. The radio lags the X-rays by about 12 days. If this implies there is a coupling between thee X-ray and radio emitting mechanisms, and external emission model would not be possible. In an internal jet model, this coupling is naturally expected; that the X-ray emitting disk is connected to the source of the radio photons (Alexander et al., 2016). Each of these models for radio emission is still being explored, and with more radio detections of TDEs, our understanding of the emitting mechanism will improve.

Taken together, multi-wavelength observations provide convincing evidence for tidal disruption flares in rough agreement with our first-order theoretical picture. My work aims to use our theoretical models, along with simulation data to improve our understanding of these observations and characteristics of TDEs.

1.2.3 Optical/Utlraviolet

In the last decade, several transients discovered in optical and ultraviolet wavelengths have been attributed to TDEs. TDE flares were initially predicted to be brightest in X-rays, due to the high temperature of an accretion disk, and subsequently the earliest TDEs were detected in the X-ray, as mentioned in Section 1.2.1. However, the optically-discovered TDES have shown to have surprisingly diverse X-ray properties. Their optical X-ray to optical emission ratios at maximum light range from $\gtrsim 10^3$ to $< 10^{-3}$ (Auchettl et al., 2017). Producing such luminous optical emission without significant X-ray flux can be explained in one of two ways: either X-ray faint TDEs are powered primarily by stream collisions rather than accretion, or the accretion disk emission is reprocessed through an atmosphere (Nicholl et al., 2020). A critical question in TDE research is what the mechanism is that is powering this implied reprocessing layer.

The messy geometry of the debris from a TDE makes this question a difficult one. Colliding streams, inflowing and outflowing gas, and a viewing-angle dependence on both the broad-band (Dai et al., 2018) and spectroscopic (Nicholl et al., 2019) properties are all pieces that come together and create a tangled geometry web. As mentioned in Section 4.2, radio observations from a growing sample of TDEs can give us a clue on the reprocessing mechanism because we can measure the properties (energy, velocity, and density) of an outflow directly using their observed radio emission. One proposed mechanism of the observed radio emission from TDEs is an outflow of material. A number

of radio-quiet TDEs have exhibited indirect evidence for slower outflows in the form of blueshifted optical/UV emission and absorption lines (Roth & Kasen, 2018; Hung et al., 2019a,a) suggesting that outflows may be common.

Nicholl et al. (2020) go into depth on the observational properties of AT2019qiz, specifically to determine if the large optical to X-ray ratio in this TDE is due to an outflow. AT2019qiz is described as a faint-and-fast TDE because it has a peak luminosity of $L = 3.6 \times 10^{43} \mathrm{ergs}^{-1}$, which is among the lowest measured for a TDE to date. It is categorized as "fast" because of its fast optical rise. The light curve rise begins ≈ 29 days before maximum light, peaking when the photosphere reaches the radius where optical photons can escape. Nicholl et al. (2020) suggests that the rapid rise and decline of the light curve suggests that the properties of the outflows may be key to understanding the fastest TDEs. Another "faint-and-fast" TDE is iPTF16fnl (Nicholl et al., 2020). iPTF16fnl is similar to AT2019qiz in the early phase, when the dynamics of the outflow control the light curve evolution. Nicholl et al. (2020) suggest that these events may be more common at lower SMBH mass, as the escape velocity from the tidal radius scales as $v_{esc} \propto M_{\mathrm{BH}}^{1/3}$, meaning an outflow can escape more easily at low M_{BH}. This is just one example why understanding the properties of these outflows could be essential in determining properties of the SMBH.

By constructing the bolometric light curve of AT2019qiz, Nicholl et al. (2020) fit a blackbody function to estimate the temperature, radius, and missing energy outside of the observed wavelength range. Most significant to following sections, the result was that the blackbody radius grows linearly up to maximum light, with a best-fit velocity of 2200 km/s.

As mentioned in the previous section, the expected decline rate of the post-disruption mass return flow follows a decay of $t^{-5/3}$. Optical-ultraviolet TDEs follow this decay on

timescales of weeks to months after reaching a peak blackbody luminosity around 10^{44} erg/s.

Classifying optical/UV flares as TDEs is not straightforward due to the difficulty in distinguishing them from AGN light. The first instrument to detect an optical-UV candidate TDE was the Galaxy Evolution Explorer (GALEX) (Martin et al., 2005). All three TDEs found in GALEX data have relatively high blackbody temperatures (T $\approx 5 \times 10^4$K), making them stand out from AGN flares. The GALEX transient search has been the only UV based TDE search to date, however optical surveys have led to the discovery of TDEs that can be classified based on their spectral properties.

The Sloan Digital Sky Survey (SDSS) (York et al., 2000) have found two types of TDE candidates. First, the SDSS catalog of galaxy spectra (Strauss et al. 2002) enabled the discovery of coronal-line TDEs (van Velzen et al., 2020). For these sources, the TDE is not observed directly, but rather transient narrow high-ionization emission lines are seen, and are interpreted as an "echo" of a soft X-ray flare (required to produce the coronal lines) originating in a TDE. While this method shows great promise as a way to detect TDEs themselves, van Velzen et al. (2020) notes that due to a lack of multi-epoch imaging observations that cover the flare itself, our knowledge of properties (such as timescales, location, blackbody temperature) of these events is limited.

SDSS also provided the first TDE candidates using optical imaging observations (van Velzen et al., 2011). Observations were taking at a cadence of a few days for three months from 2005 to 2007 which yielded two events classified as TDEs. The key property distinguishing these flares from normal supernovae and AGN is a high blackbody temperature (as measured using SDSS ugri photometry) that remained constant for at least three months (van Velzen et al., 2020).

The Pan-STARRS medium deep survey (Chambers et al., 2016) detected a TDE (PS1-

10jh) from a non-AGN galaxy with multiple pre-peak detections and multiple spectroscopic observations. As expected, it showed transient ultraviolet emission (detected by GALEX) and long-term high blackbody temperatures. Because of the pre-peak detections, PS1-19jh became the main archetype for the optical-ultraviolet class of TDEs. Spectroscopic signatures of these optical/uv TDEs show broad He and/or H emission.

Data sets such as the Palomar Transient Factory (PTF) (Law et al., 2009) have identified multiple TDEs by searching for spectroscopically-observed nuclear flares. Several TDEs were identified this way with relatively high blackbody temperatures, and similar spectroscopic signatures as PS1-19jh. Additionally, the iPTF (Hung et al., 2018) search for TDES used properties of previous TDEs to identify new candidates in real time, maximizing the advantage of follow-up data in real time and finding a total of three TDE candidates.

One of the most successful searches for optical/UV TDEs was done with the All Sky Automated Survey for supernovae (ASAS-SN) (Shappee et al., 2014). ASAS-SN currently consists of 24 telescopes, distributed around the globe and is automatically surveying the entire visible sky every night down to about 18th magnitude, more than 50,000 times deeper than human eye. ASAS-SN has found eight TDEs to date, with identification established via spectroscopic follow-up. ASAS-SN is sensitive to closer TDES ($z \sim 0.03$), making them ideal for followup observations at different wavelengths. For example, ASASSN-14li is the first optical TDE with a well-sampled X-ray light curve, with detections also in the radio (van Velzen et al., 2016).

Other surveys that have detected optical TDEs are the Asteriod Terrestrial-impact Last Alert System (ATLAS) (Tonry et al., 2018), the Optical Gravitational Lensing Experiment (OGLE) (Wyrzykowski et al., 2014), and the Zwicky Transient Facility (ZTF) (Bellm et al., 2019). ZTF started in early 2018 and is still running. To date, the largest sample of op-

tically selected TDEs comes from ZTF with a sample of 30 TDEs total. These TDEs also have follow-up Swift UV observations and X-ray observations, getting us closer to understanding the entire picture of a TDE.

The future of optical/UV TDE discovery is very bright. The 10-year Legacy Survey of Space and Time (LSST) is set to take its first light in July 2024. The Rubin Observatory LSST is designed to address probing dark energy and dark matter, taking inventory of the solar system, mapping the Milky Way, and most important for TDEs: exploring the transient optical sky. (SST will observe 18000 deg^2 of the Southern sky and is expected to discover thousands of transients every night due to its large coverage area and its observing strategy. LSST will observe in six optical bands, u, g, r, i, z and y, covering the wavelength range between 320 and 1050 nm. Bricman & Gomboc (2020) used the LSST simulation framework and defined TDE catalogs to estimate the possible number of TDEs to be detected over the 10-year LSST survey. They looked at six SMBH mass distributions, and found an average of between 35,000 and 80,000 TDES to be detected. They do note that it will be a difficult task to distinguish TDEs from other transients, so this number will decrease. However, this survey will exponentially increase the number of observed TDEs, making this an exciting time for TDE research.

1.3   MECHANICS OF A TIDAL DISRUPTION EVENT

To look closer at the mechanics of a tidal disruption event, we start with Newtonian physics. If a star within a galactic nuclei with mass M_* and radius R_* is perturbed on a radial orbit, it will eventually come into contact with its central SMBH of mass M_{BH}.

The key length-scale in the TDE is the tidal radius, which is

$$r_{\mathrm{T}} = \left(\frac{M_{\mathrm{BH}}}{M_*} \right)^{1/3} R_*, \tag{1.1}$$

where M_{BH} is the mass of the black hole, M_* is the mass of the star, and R_* is the radius of the star. We define $\alpha = (M_{\mathrm{BH}}/M_*)^{1/3}$. Following Guillochon & Ramirez-Ruiz (2013), we define the penetration ratio, β as

$$\beta \equiv \frac{r_{\mathrm{T}}}{r_{\mathrm{p}}}, \tag{1.2}$$

where r_{p} is the periapse.

We note here that the tidal radius scales as $M_{\mathrm{BH}}^{1/3}$ where the Scharzchild radius, or radius of the event horizon scales linearly with M_{BH}

$$R_s = \frac{2GM_{\mathrm{BH}}}{c^2} \tag{1.3}$$

Therefore, above a critical mass of

$$M_{c,BH} = 1.1 \times 10^8 M_\odot \left(\frac{R_*}{R_\odot}\right)^{3/2} \left(\frac{M_*}{M_\odot}\right)^{-1/2} \tag{1.4}$$

the star will be completely swallowed into the SMBH prior to a TDE.

Assuming a (near-) Keplerian potential, the velocity of a star on a zero energy orbit at r_{T} is

$$v_{\mathrm{T}} = \sqrt{\frac{2GM_{\mathrm{BH}}}{r_{\mathrm{T}}}} = \alpha v_*, \tag{1.5}$$

where G is Newton's constant and $v_* = \sqrt{2GM_*/R_*} = 437\,(M_*/1\,M_\odot)^{1/2}(R_*/1\,R_\odot)^{-1/2}\,\mathrm{km\,s^{-1}}$ is the escape velocity from the star. This quantity turns out to be a useful quantity to write

other quantities in. For instance, the velocity at periapse is then:

$$v_{\mathrm{p}} = \sqrt{\frac{GM}{r_{\mathrm{p}}}} = \sqrt{\beta} v_{\mathrm{T}} = \sqrt{\beta} \alpha v_*. \tag{1.6}$$

The specific angular momentum associated with a zero energy orbit is:

$$l = v_{\mathrm{p}} r_{\mathrm{p}} = \frac{v_{\mathrm{T}} r_{\mathrm{T}}}{\sqrt{\beta}} = \frac{v_* R_* \alpha^2}{\sqrt{\beta}}. \tag{1.7}$$

In the above, we have assumed that $M_{\mathrm{BH}} \gg M_*$. Thus, the initial velocity can be broken into a radial component $v_{0,\parallel}$ and a perpendicular component $v_{0,\perp}$ with values:

$$v_{0,\perp} = \frac{l}{r_0} = \frac{\alpha v_*}{\eta\sqrt{\beta}} \quad \text{and} \quad v_{0,\parallel} = \sqrt{v_0^2 - v_{0,\perp}^2} = \alpha v_* \sqrt{\frac{\eta\beta - 1}{\eta^2\beta}}, \tag{1.8}$$

where $\eta = r_0/r_{\mathrm{T}}$ is the dimensionless starting radius, and r_0 is starting radius of the star's orbit.

1.4 DYNAMICS OF DISRUPTION

The penetration parameter, β will determine if the star is partially or completely disrupted. A star will be completely disrupted for $\beta \geq 2$. When this happens, half of the debris will remain bound to the SMBH while the other half will be unbound in space.

The gravity of the BH and the gravity of the star is:

$$F_{g,BH} = \frac{GM_{BH}}{r^2} \quad \text{and} \quad F_{g,*} = \frac{Gm}{r_*^2} \tag{1.9}$$

The tidal gravity of the BH is the difference in the gravity pull on one side versus

13

another

$$F_{g,BH,1} = \frac{GM_{BH}}{(r - r_*)^2} \quad \text{and} \quad F_{g,BH,2} = \frac{GM_{BH}}{(r + r_*)^2} \tag{1.10}$$

So the difference is

$$\Delta F = F_{g,BH,1} - F_{g,BH,2} \tag{1.11}$$

Assume $r_* \ll r$, so we Taylor expand

$$\Delta F = \frac{2GM_{BH}r_*}{r^3} \tag{1.12}$$

Equate this to the self-gravity of the star

$$\Delta F = F_{g,*} \rightarrow \frac{2GM_{BH}r_*}{r^3} = \frac{Gm}{r_*^2} \rightarrow \left(\frac{r_*}{r}\right)^3 = \frac{m}{M_{BH}} \tag{1.13}$$

This defines r_T or the tidal radius

$$r_T = r_* \left(\frac{M_{BH}}{m}\right)^{1/3} \tag{1.14}$$

If $r < r_T$, the star is ripped apart.

Assuming the star is on a zero energy orbit, we can calculate the velocity of the star.

$$E = 0 = KE + PE = \frac{1}{2}mv_{orb}^2 - \frac{GM_{BH}m}{r} \rightarrow \frac{1}{2}mv_{orb}^2 = \frac{GM_{BH}m}{r} \tag{1.15}$$

14

So this gives $v_{orb} = \sqrt{2GM_{BH}/r}$. Then at $r = r_T$ the velocity of the star is

$$v_{orb} = \sqrt{\frac{2GM_{BH}}{r}} \tag{1.16}$$

At closest approach, the binding energy of the part of the star closest to the BH will be

$$E_1 = KE_1 + PE_1 = \frac{1}{2}mv_{orb}^2 - \frac{GM_{BH}m}{(r_T - r_*)} \tag{1.17}$$

And the part of the star furthest to the BH:

$$E_1 = KE_1 + PE_1 = \frac{1}{2}mv_{orb}^2 - \frac{GM_{BH}m}{(r_T + r_*)} \tag{1.18}$$

By Taylor expanding E_1 and E_2 with $r_* \ll r_T$ we can calculate the energy on either side of the star to be:

$$E_{1,2} = \pm \frac{Gm}{r_*} \left(\frac{M_{BH}}{m}\right)^{1/3} \tag{1.19}$$

Showing that half of the star remains bound with the other half will be unbound.

Now we move to deriving the fallback rate, $\frac{dM}{dE}$, of the material from the disrupted star onto the black hole.

Consider an object orbiting a massive body such as a BH. If it is in a circular orbit:

$$\frac{mv^2}{r} = \frac{GM_{BH}m}{r^2} \tag{1.20}$$

The time it takes to complete one orbit will be

$$t = \frac{d}{v} = 2\pi\sqrt{\frac{r^3}{GM_{BH}}} \tag{1.21}$$

Using $E = -\frac{1}{2}\frac{GM_{BH}m}{r}$, we can write r in terms of E, and then t in terms of E:

$$t = 2\pi GM_{BH}\left(\frac{|E|}{m}\right)^{-3/2} \tag{1.22}$$

Finally, we arrive at the equation for our fallback rate of the bound material:

$$\frac{dM}{dt} = \frac{dM}{dE}\frac{dE}{dt} = \frac{(2\pi GM_{BH})^{2/3}}{3}\frac{dM}{dE}t^{-5/3} \tag{1.23}$$

We can calculate the maximum penetration parameter that leads to a stable orbit by finding the inner most stable orbit, or ISCO, for a SMBH. We define the ISCO as R_S. For a $10^6 M_\odot$ black hole, this gives us an ISCO of

$$r = 3 \times 10^{11}\left(\frac{M_{BH}}{10^6 M_\odot}\right)\text{cm} \tag{1.24}$$

Using this as our distance of closest approach, we can calculate a maximum β of 8 for a SMBH with a mass of $10^6 M_\odot$. Knowing this, our research dives more in depth in conclusions made for TDEs with $\beta \leq 8$.

CHAPTER 2

Moving Mesh Hydrodynamics

Two numerical methods that have been instrumental in simulating astrophysical phenomena and have paved the way for moving-mesh codes are smoothed-particle hydrodynamics (SPH) and Eulerian grid codes. These methods have been used to simulate and study events such as stars, galaxies, accretion disk, common envelope evolution and more. Each method has its own strengths and weaknesses. Recently, a new numerical method has been developed that meshes the SPH and Eulerian methods together, trying to preserve the strengths of each. This method is called the arbitrary Lagrangian-Eulerian (ALE) method. To begin this chapter, we will describe each of these two methods in depth, and arrive at the intersection of the two in the moving-mesh method.

2.1 SMOOTHED-PARTICLE HYDRODYNAMICS

2.1.1 Overview

The basic form of smoothed particle hydrodynamics (SPH) was introduced over 40 years ago by Gingold & Monaghan (1977) and Lucy (1977) and has become a popular method due to its application to a wide range of astrophysical processes such as accretion disks, stellar collisions, and star formation. Common SPH codes to study these processes are GADGET (Springel et al., 2001), HYDRA (Pearce & Couchman, 1997), and MAGMA (Rosswog, 2007). The SPH code ChaNGa (Jetley et al., 2008, 2010; Menon et al., 2015) is the SPH code that forms the basis of MANGA that we will discuss in detail in Section 2.4.

SPH is a Lagrangian scheme that is based on particle interpolation to compute smooth field variables. These particles are more so carriers of physical properties such as mass,

density, volume, velocity, etc. than physical particles themselves. This means that SPH codes model the fluid as a collection of fixed-mass particles whose properties evolve according to the Euler equations. The properties of each particle are calculated from a weighted average of the values on other local particles. In this manner each particle is essentially "smoothed" over a finite volume of fixed mass, and in this way SPH is naturally adaptive with density.

2.1.2   Formalism

At the heart of SPH is an interpolation method which allows any function to be expressed in terms of its values at a set of disordered points, which we define as "particles" (Gingold & Monaghan, 1977).

The integral interpolant of any function $F(\mathbf{r})$ used to smooth the function $F(\mathbf{r})$ to a smoothed field, $F_s(\mathbf{r})$ is

$$F_s(\mathbf{r}) = \int F(\mathbf{r}')W(\mathbf{r} - \mathbf{r}', h)\mathbf{dr}' \tag{2.1}$$

where the integration is over the entire space, and W is an interpolating kernel. The kernel has characteristic width h, known as the smoothing length. The smoothing length h determines the resolution and is proportional to the local particle spacing.

The integral interpolant in Equation 2.1 can be approximated by splitting the fluid into small volume elements ΔV each with mass $\rho\Delta V$, where ρ is a representative density for the small fluid element. With this, we can use Equation 2.1 on our discrete distribution of particles $F_a(\mathbf{r}_a)$ with

18

$$F_{s,a}(\mathbf{r}_a) = \sum_b \frac{m_b}{\rho_b} F(\mathbf{r}_b) W(\mathbf{r}_a - \mathbf{r}_b, h_a) \tag{2.2}$$

where the summation is over the particles of mass m_b, position $\mathbf{r}_b$ and density ρ_b.

The goal of the code is to solve the equations of motion. The SPH code will do this by using the Euler-Lagrange equations of motion. The Euler equations for gas dynamics in Lagrangian form are

$$\frac{D\rho}{Dt} = -\rho \boldsymbol{\nabla} \cdot \mathbf{u} \tag{2.3}$$

$$\frac{D\mathbf{u}}{Dt} = -\frac{\boldsymbol{\nabla} P}{\rho} \tag{2.4}$$

$$\frac{De}{Dt} = -\frac{P}{\rho} \boldsymbol{\nabla} \cdot \mathbf{u} \tag{2.5}$$

where ρ, $\mathbf{u}$, P, and e are the fluid's density, velocity, pressure and internal energy. Additionally, $\frac{D}{Dt} = \frac{\partial}{\partial t} + \mathbf{u} \cdot \boldsymbol{\nabla}$. Equations 2.3, 2.4, 2.5 represent the conservation of mass, momentum and energy respectfully.

With these, the Lagrangian

$$L = \int \rho \left(\frac{1}{2} \mathbf{u}^2 - e \right) dV \tag{2.6}$$

19

can be solved in discretized (SPH) form:

$$L = \sum_b m_b \left(\frac{1}{2} \mathbf{u}_b^2 - e_b) \right) \tag{2.7}$$

Then the Euler-Lagrange equation can be used to derive the SPH equations of motion.

2.1.3 Artificial Viscosity

Because of its smoothing nature, shock waves and contact discontinuities are a problem for SPH codes. In SPH, a discontinuity is smeared out across several particles, creating poor gradient estimates. To counteract this, SPH introduces an artificial viscosity. The method of adding an artificial viscosity (AV) works as applying a friction force to damp the relative motion of the particles.

The AV is implemented by solving a momentum equation of the form:

$$\frac{d\boldsymbol{u}_i}{dt}\Big|_{visc} = -\sum_{j=1}^{n} m_j \left(\frac{P_i}{\rho_i^2} + \frac{P_j}{\rho_j^2} + \Pi_{ij} \right) \boldsymbol{\nabla} W_{ij} \tag{2.8}$$

Here W_{ij} is

$$W_{ij} = W(|\mathbf{r}_i - \mathbf{r}_j|, h_i) \tag{2.9}$$

P_j is pressure, $\boldsymbol{u}_i$ is velocity and the viscosity term Π_{ij} is given by

$$\Pi_{ij} = \begin{cases} \frac{-\alpha \frac{1}{2}(c_i + c_j)\mu_{ij} + \beta \mu_{ij}^2}{\frac{1}{2}(\rho_i + \rho_j)}, & \text{for } \boldsymbol{u}_{ij} \cdot \boldsymbol{r}_{ij} < 0 \\ 0, & \text{otherwise} \end{cases} \tag{2.10}$$

where $r_{ij} = r_i - r_j$, $u_{ij} = u_i - u_j$, c_j is the sound speed and μ_{ij} is a function of the smoothing length h, u_{ij} and r_{ij}. α and β are the coefficients used for setting the viscosity strength. The commonly used values in the literature is α = 1 and β = 2 which was proposed by Lattanzio (1986) using Sod shock tube tests. The smoothing length in Equation 2.9 is chosen to be the same for each particle to keep the term symmetric. The right hand side of Equation 2.8 is symmetric in order to obey Newton's third law. Note that the viscosity term Π_{ij} vanishes for $u_{ij} \cdot r_{ij} > 0$, meaning it only applies to approaching particles.

Any momentum lost by one particle due to equation 2.8 will be gained by another, preserving momentum conservation. While AV aids in the difficulty of shock resolution, it adds its own set of problems. Studies such as Agertz et al. (2007) and Dolag et al. (2005) have found that artificial viscosity dampens small scale velocities perturbations and creates diffusion of post shock vorticity and thus smearing of turbulence. In the following section, we will discuss a method that can sharply resolve the location of a discontinuity.

2.2 EULERIAN GRID SCHEMES

Opposite of the Lagrangian viewpoint, the Eulerian formulation of fluids watches the flow of a fluid past a static point of reference in space. The Eulerian method discretizes the fluid and has a mesh of cells which are fixed in space and allow the fluid to flow through it. The mesh can be cartesian, cylindrical, spherical or a different geometry depending the best model for the problem. The Eulerian grid method allows the application of finite-volume methods to solve the Euler equations instead of solving the Euler equations for a group of particles like in SPH. For this reason, the Eulerian method is superior at modeling shocks and other discontinuities. Common Eulerian grid-based codes are

FLASH (Fryxell et al., 2000), RAMSES (Teyssier, 2002), and Athena (Stone et al., 2008).
Eulerian grid-based codes are used to model phenomena such as X-ray bursts, classical
novae, supernovae, just to name a few.

The Euler equations written in conservative form are

$$\frac{\partial \rho}{\partial t} + \boldsymbol{\nabla} \cdot (\rho \mathbf{u}) = 0 \tag{2.11}$$

$$\frac{\partial \rho \mathbf{u}}{\partial t} + \boldsymbol{\nabla} \cdot (\rho \mathbf{u} \mathbf{u}^T) + \boldsymbol{\nabla} P = -\rho \boldsymbol{\nabla} \Phi \tag{2.12}$$

and

$$\frac{\partial \rho e}{\partial t} + \boldsymbol{\nabla} \cdot (\rho e + P) \mathbf{u} = -\rho \mathbf{u} \cdot \boldsymbol{\nabla} \Phi \tag{2.13}$$

where ρ is the density, $\mathbf{u}$ is the fluid velocity, Φ is the gravitational potential, $e = \epsilon + u^2/2$
is the specific energy, ϵ is the specific internal energy, and $P(\rho, \epsilon)$ is the pressure. Equations
2.11, 2.12, 2.13 can be written in a compact form by defining a state vector $\mathcal{U} = (\rho, \rho \mathbf{u}, \rho e)$:

$$\frac{\partial \mathcal{U}}{\partial t} + \boldsymbol{\nabla} \cdot \boldsymbol{\mathcal{F}} = \boldsymbol{\mathcal{S}} \tag{2.14}$$

where $\boldsymbol{\mathcal{F}} = (\rho \mathbf{u}, \rho \mathbf{u} \mathbf{u}^T + P \mathbb{1}, (\rho e + P) \mathbf{u})$ is the flux function and $\boldsymbol{\mathcal{S}} = (0, -\rho \boldsymbol{\nabla} \Phi, -\rho \mathbf{u} \cdot \boldsymbol{\nabla} \Phi)$
is the source function. Here $\mathbb{1}$ is the identity matrix.

For each cell, the integral over the volume of the ith cell defines the charge of the ith

cell, $\boldsymbol{U}_i$, to be

$$U_i = \int_i \boldsymbol{\mathcal{U}}dV = \boldsymbol{\mathcal{U}}_i V_i, \tag{2.15}$$

where V_i is the volume of the cell. As in S10, we then use Gauss' theorem to convert the volume integral over the divergence of the flux in equation (5.1) to a surface integral:

$$\int_i \boldsymbol{\nabla} \cdot \boldsymbol{\mathcal{F}}dV = \int_i \boldsymbol{\mathcal{F}} \cdot \hat{\boldsymbol{n}}dA \tag{2.16}$$

We now take advantage of the fact that the volumes are Voronoi cells with a finite number of neighbors to define a integrated flux

$$\sum_{j \in \text{neighbors}} \boldsymbol{F}_{ij} A_{ij} = \int_i \boldsymbol{\mathcal{F}} \cdot \hat{\boldsymbol{n}}dA, \tag{2.17}$$

where $\boldsymbol{F}_{ij}$ and A_{ij} are the average flux and area of the common face between cells i and j. The discrete time evolution of the charges in the system is given by:

$$\boldsymbol{U}_i^{n+1} = \boldsymbol{U}_i^n + \Delta t \sum_j \hat{\boldsymbol{F}}_{ij} A_{ij} + \Delta t \boldsymbol{S}_i, \tag{2.18}$$

where $\hat{\boldsymbol{F}}_{ij}$ is an estimate of the half-time-step flux between the initial, $\boldsymbol{U}_i^n$, and final states $\boldsymbol{U}_i^{n+1}$ and $\boldsymbol{S}_i^{(n+1/2)} = \int_i \boldsymbol{\mathcal{S}}dV$ is the time-averaged integrated source function. The flux and source function are determined at the half-time-step so that the algorithm achieves second-order accuracy in time.

We estimate the flux across each face, $\hat{\boldsymbol{F}}_{ij}$, using an approximate Riemann solver. The Riemann solver uses the state $\boldsymbol{\mathcal{U}}$ and flux $\boldsymbol{\mathcal{F}}$ on each side of the cell on each side of the cell interface to solve the Euler equations. Some of the most common Riemann solvers are the

Harten-Lax-van Leer-Contact (HLLC), Harten-Lax-van Leer (HLL), and Harten-Lax-van Leer with contact and Alfven mode (HLLD). The HLL or HLLC solver is typically used for hydrodynamics, while the HLLD solver is used for magneto-hydrodynamics.

The HLL solver ignores the middle states and decomposes $\mathcal{U}$ into two states. This gives us a left state $\mathcal{U}_{L,}^{n+1/2} = \mathcal{U}^n$, a right state, $\mathcal{U}_R^{n+1/2} = \mathcal{U}^{n+1}$, and a middle state $\mathcal{U}_M^{n+1/2}$:

$$\mathcal{U}_M = \frac{\mathcal{S}_R \mathcal{U}_R - \mathcal{S}_L \mathcal{U}_L + \mathcal{F}_L - \mathcal{F}_R}{\mathcal{S}_R - \mathcal{S}_L} \tag{2.19}$$

Where we dropped the $n+1/2$ for notation convenience. The state $\mathcal{U}_M$ is now the state at the interface. $\mathcal{S}_R$ and $\mathcal{S}_L$ are the speeds that the state propagates outwards at from the right and the left, respectfully. Using the above expressions one can derive that the flux at the interface is then

$$\mathcal{F}^{n+1/2} = \begin{cases} \mathcal{F}^n, & \text{if } \mathcal{S}_L \geq 0 \\ \frac{\mathcal{S}_R \mathcal{F}^n - \mathcal{S}_L \mathcal{F}^{n+1} + \mathcal{S}_R \mathcal{S}_L (\mathcal{U}^{n+1} - \mathcal{U}^n)}{\mathcal{S}_R - \mathcal{S}_L}, & \text{if } \mathcal{S}_L < 0 < \mathcal{S}_R \\ \mathcal{F}^{n+1}, & \text{if } \mathcal{S}_R \leq 0 \end{cases} \tag{2.20}$$

where $\mathcal{S}_L$ and $\mathcal{S}_R$ are chosen to be the fastest signal speeds of each initial state. One of the main disadvantages of this HLL solver is that it cannot keep discontinuities sharp. This is not surprising since there is no middle state in this scheme.

A newer version of the HLL scheme is the HLLC scheme, where the C stands for contact wave (state): this is a method which does include the middle state that is missing from the standard HLL scheme. The general way to construct this scheme is the same as shown above. Instead of 2 waves ($\mathcal{S}_L$ and $\mathcal{S}_R$) and 3 regions of constant $\mathcal{U}$ we now have 3 waves and 4 regions of constant $\mathcal{U}$. This is done by using a third wave $\mathcal{S}_*$ that splits

the interaction region into two partitions $\mathcal{U}_{*,L}$ and $\mathcal{U}_{*,R}$. Toro et al. (1994) goes into more depth on the HLLC solver.

Eulerian grid codes also offer adaptive mesh resolution with adaptive mesh refinement (AMR) techniques. AMR is a method of adapting the accuracy of a solution within certain sensitive or turbulent regions of simulation. For each level of refinement, each cell is split into its eight octants (in 3-D) or four quadrants (in 2-D), which inherit properties based on the cell-centered values and gradients of its parent cell. The advantage of using AMR is shown in Figure 2.1.

The Eulerian grid method also has its downfalls. Since the discretization of the simulation domain does not change with the material shape, interface tracking and moving boundaries are problematic in Eulerian simulations. Eulerian grids also suffer from a lack of Galilean-invariance, making their results sensitive to bulk velocities. This is a source of substantial concern in simulations of galaxy formation, where galaxies move with large speeds relative to each other, speeds that are often orders of magnitude larger than the sound speed of the dense interstellar medium that one wants to follow hydrodynamically (Springel, 2010). In the case of AMR, there may be overmixing if the resolution is limited or the bulk velocities are large (Springel, 2010).

2.3 ARBITRARY LAGRANGIAN-EULERIAN SCHEMES

One proposed solution to the withstanding downfalls mentioned in Sections 2.1 and 2.2 is to let the mesh itself move and deform along with the fluid. The first attempt at this was by Whitehurst (1995) with their code FLAME. FLAME aimed to combine the finite-volume methods of a Eurlerian grid with the Galilean invariance, lack of preferred axes, and automatic resolution adjustment of Lagrangian methods. This hybrid method is called the arbitrary Lagrangian-Eulerian (ALE) scheme. The codes using ALE schemes
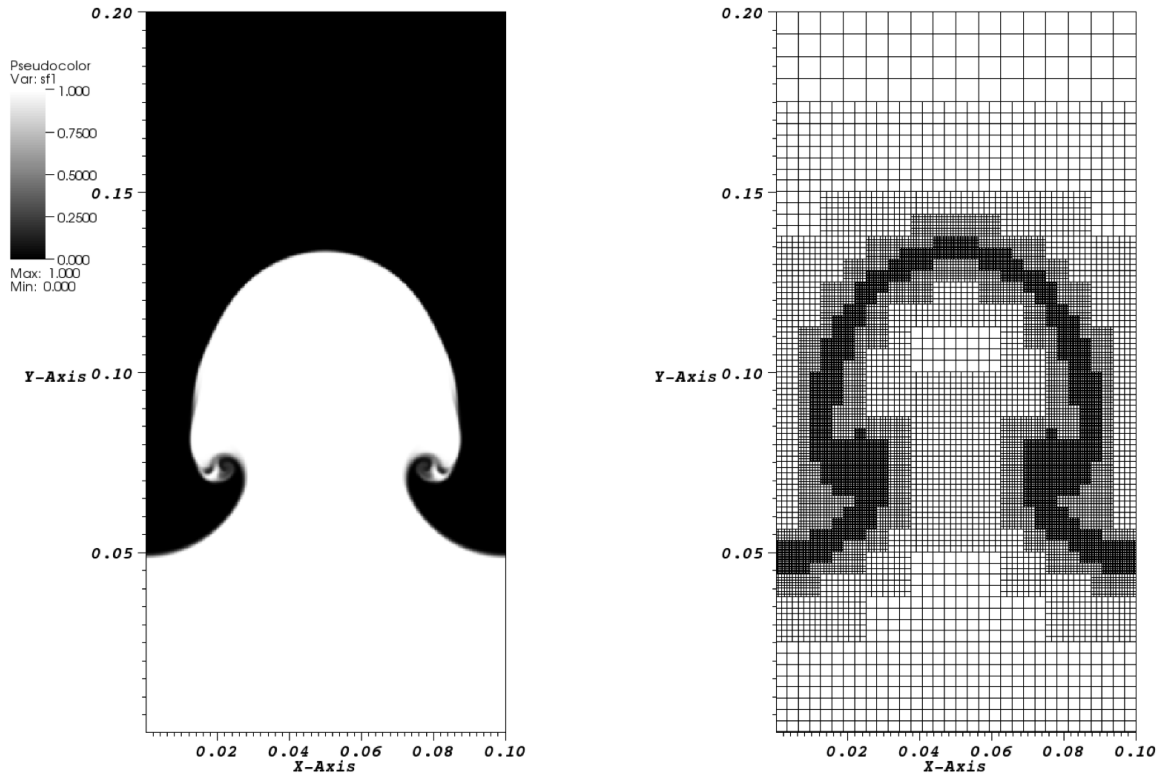
Figure 2.1: (Left) Grayscale image of the concentration of a passively-advected contaminant at late time in the magnetic Rayleigh-Taylor instability using the code Athena in Stone et al. (2008). (Right) Grid blocks used to resolve the interface using AMR.

were categorized as moving-mesh (MM) codes because the mesh would move with the fluid. A simple illustration of the differences in SPH, Eulerian, and ALE methods is shown in Figure 2.2.

Gnedin (1995) and Pen (1998) have presented moving-mesh algorithms that have been successful for a range of cosmological problems, however this method relies on the continuous deformation of a Cartesian grid. This results in the mesh becoming heavily distorted. In general, mesh tangling (manifested in 'bow-tie' cells and hourglass like mesh motions) is the traditional problem of multi-dimensional Lagrangian hydrodynamics. To counteract this, remapping techniques to regular meshes were introduced to allow the mesh to continue past the point it would have been twisted. This seems like a simple solution, but a general re-mapping technique that could generate a mesh appropriate to a range of problems is not straightforward. Springel (2010) proposed a new formulation of continuum hydrodynamics based on an unstructured mesh. The mesh is defined as the Voronoi tessellation of a set of discrete mesh generating points, which are in principle allowed to move freely. This scheme is implemented and has been proven successful in the code AREPO (Springel, 2010).

2.3.1   Voronoi Tessellations

For a given set of points, Springel (2010) defined a Voronoi tessellation as a space consisting of non-overlapping cells around each of the sites such that each cell contains the region of space closer to it than any of the other sites. In other words, for a given mesh-generating point, its Voronoi cell is defined as the set of all points which are closer to it than any other mesh-generating point (shown in Figure 2.3). After generating the Voronoi tessellation, the Euler equations (2.11, 2.12, 2.13) can be solved the same as in the Eulerian grid scheme. The advantages of using a Voronoi tessellation are that the tessellation
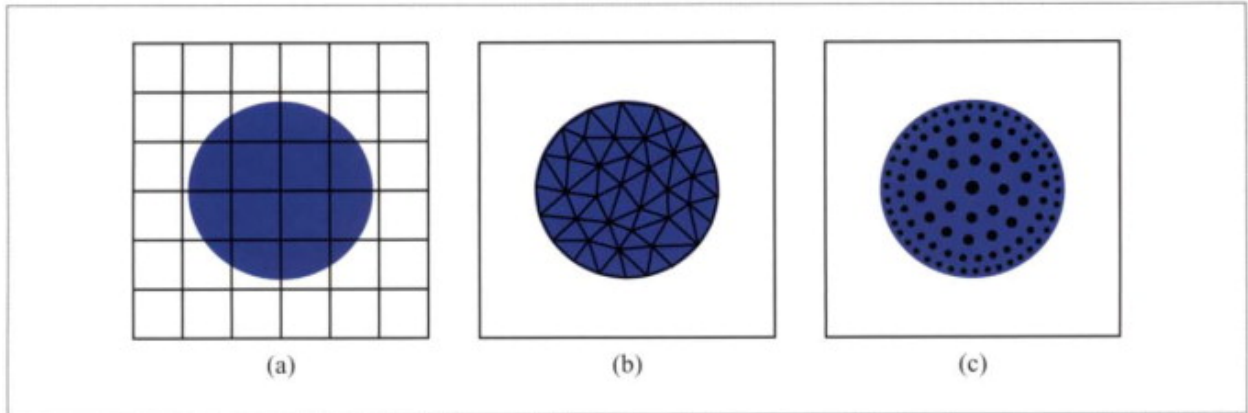
Figure 2.2: A 2D sphere of blue material discretized in a Eulerian mesh (a), Lagrangian mesh (ALE scheme) (b), and using particles (c). The Lagrangian elements discretize only the material, while the Eulerian elements discretize the embedding space. Only the meshes define a disjoint partitioning of space. The ALE scheme (b) shows a hybrid of the Eulerian mesh and Lagrangian particle methods. Reprinted from Matthias et al. (2007).

is unique to the distribution of mesh generating points, and the tessellations deforms smoothly under perturbations of the positions of the mesh generating points.

One way to create the Voronoi tessellation is by first starting with the Delauney tessellation. The Delauney tessellation for a given set of points is a triangulation of the plane, where the points serve as vertices of the triangles as shown in Figure 2.3. The rule that defines the Delaunay triangulation is that each circumcircle around one of the triangles of the tessellation is not allowed to contain any of the other mesh-generating points in its interior. In 3-D, this results in tetrahedral cells with mesh-generating points at their vertices where the tetrahedra are not allowed to contain any of the points inside their circumspheres. In Figure 2.3, it is shown that the sides of the tetrahedra in the Voronoi tessellation are at the midpoint between two mesh generating points. The Delauney tessellation is the topological dual to the Voronoi tessellation. This means that with one, the other can be created. In the code AREPO described in detail in Springel (2010), the Delauney tessellation is created first and the Voronoi tessellation is created from it.

28

The second way the Voronoi tessellation can be generated is by computing it directly. The moving-mesh code MANGA (discussed in detail in Section 2.4) computes the Voronoi tessellation directly using the publicy-available VORO++ libraries. The algorithm in VORO++ uses a nearest neighbor search. The steps to computing the Voronoi cell about a mesh-generating point directly are:

1. Create an arbitrary large cell around the point, much larger than the spacing between particles.

2. Using a rapid nearest-neighbor search algorithm, we can search for all neighbors n up to a radius r_s, which we will presume is arbitrary. The neighbors around the point are ordered by distance to the point.

3. The line connecting this point to its nearest neighbor is computed.

4. The plane bisecting this line is computed.

5. The cell is split into two partitions by this plane.

6. Steps 3-5 are repeated with the next-nearest neighbor. This process is complete when the distance from the point to the nearest neighbor is more than twice the distance from the point to any vertex on the surface of the cell.

2.4 MANGA ALGORITHM

2.4.1 Overview

The scheme proposed in Springel (2010) has led to a number of ALE codes including TESS (Duffell & MacFadyen, 2011), FVMHD3D (Gaburov et al., 2012), RICH (Yalinewich
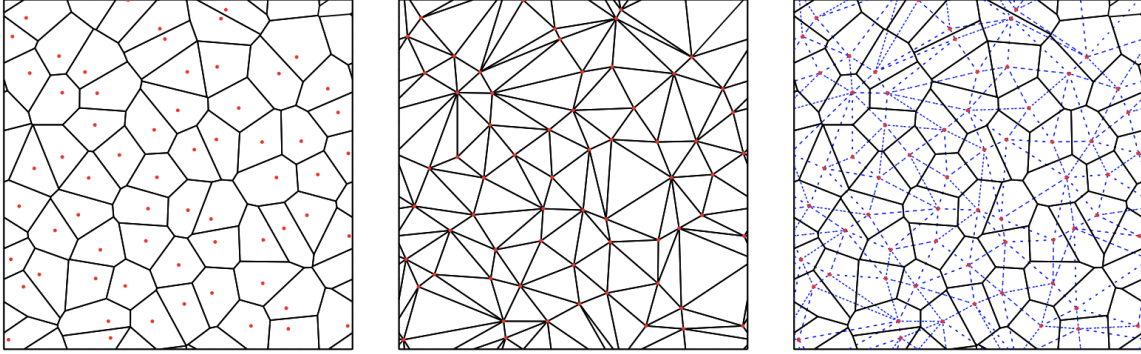
Figure 2.3: Example of a Voronoi and Delaunay tessellation in 2D, with periodic boundary conditions. The panel on the left shows the Voronoi tessellation for N = 64 points (shown as red circles), the panel in the middle gives the corresponding Delaunay tessellation, while the panel on the right shows both simultaneously (solid lines show the Voronoi, dashed lines the Delaunay tessellation (reprinted from Springel (2010)).

et al., 2015), and (Duffell, 2016). In addition, the general scheme of determining the geometry from an arbitrary collection of points has also led to derivative methods such as GIZMO (Hopkins, 2015). Both AREPO and GIZMO are built on top of the Gadget codebase (Springel, 2005), which demonstrates that SPH codes can be modified to an ALE scheme. As mentioned in Section 2.1, the SPH code ChaNGa includes a moving-mesh hydrodynamic solver, MANGA.

Chang et al. (2017) and Prust & Chang (2019) go into a detailed discussion on MANGA, but we go through a summary of the ALE algorithm in MANGA here:

1. A valid Voronoi tessellation of the mesh-generated points is generated using the VORO++ library

2. Using the volume of the Voronoi cell and the integral quantities, U_i^n, the local gradients and the half time step conserved variables U_i^{n+1} are calculated.

3. The cells drift by a half time step and the Voronoi tessellation is rebuilt.

4. The gradients and conserved variables at the half-time-step are calculated and used to reconstruct the half-time-step face-centered quantities

5. A Riemann solver is used to calculate the flux across the faces.

6. The new state U_i^{n+1} is determined from the fluxes. New velocities for the mesh generating points are determined.

2.4.2 Flux Computation

MANGA estimates the flux across each face, $\hat{F}_{ij}$, using an approximate Riemann solver, as discussed in Section 2.2. Following Springel (2010), the 1-D fluxes across each face are computed in the rest frame of that face and then collectively applied per time-step. The $\hat{F}_{ij}$ is then estimated as follows:

1. Estimate the velocity $\tilde{w}_{ij}$ of the face following Springel (2010).

2. The state vector is boosted from the "lab" frame (the rest frame of the simulation box) to the rest frame of the face to find the flux along the normal to the face.

3. Estimate the flux $\hat{F}_{ij}$ across the face using an HLLC or HLL approximate Riemann solver following Toro (2009). For magnetohydrodynamics, we use an HLLD solver as implemented in Athena++.

4. Boost the solved flux back into the "lab" frame.

We can then use the estimated fluxes to time evolve the charges, U_i, following equation 2.18.

31

2.4.3 Gradient Estimator

MANGA is a second order accurate code in time and space. To do this, it requires an appropriate estimate for the state vector at the face centers of each cell at the half timestep.

The state vector at the half timestep will be:

$$\mathcal{U}_i^{(n+1)} = \mathcal{U}_i^{(n)} + \frac{\partial \mathcal{U}_i^{(n)}}{\partial t}\frac{\Delta t}{2} \tag{2.21}$$

where $\frac{\partial \mathcal{U}_i^{(n)}}{\partial t}$ comes from equation 2.14.

The state vector on the face of the ith and jth cell on the (n+1/2)-th timestep, $\tilde{\mathcal{U}}_{ij}^{(n+1/2)}$ is then

$$\tilde{\mathcal{U}}_{ij}^{(n+1/2)} = \mathcal{U}_{ij}^{(n+1/2)} + (\tilde{r}_{ij} - c_i) \cdot \nabla \mathcal{U}_i^{(n+1/2)} \tag{2.22}$$

where c_i is the center of mass of the ith cell and $\tilde{r}_{ij}$ is the face center between cells i and j.

Equation 2.22 requires an estimate for the gradient of the state vector in the ith cell. For this, MANGA follows the procedure of Steinberg et al. (2016) who improved upon the prescription of Springel (2010) in using the Gauss-Green theorem to estimate these gradients. MANGA also includes a slope limiter, α_i^{S10} that reduces numerical oscillations near strong gradients, i.e. shocks by:

$$\langle \mathcal{U} \rangle_i^{S10} = \alpha_i^{S10} \langle \mathcal{U} \rangle_i \tag{2.23}$$

with $\boldsymbol{\alpha}_i^{S10} = \min(1, \psi_{ij})$ and

$$\psi_{ij} = \begin{cases} (\boldsymbol{\mathcal{U}}^{max} - \boldsymbol{\mathcal{U}}_i)/\Delta\boldsymbol{\mathcal{U}}_{ij}, & \text{for } \Delta\boldsymbol{\mathcal{U}} > 0 \\ (\boldsymbol{\mathcal{U}}^{min} - \boldsymbol{\mathcal{U}}_i)/\Delta\boldsymbol{\mathcal{U}}_{ij}, & \text{for } \Delta\boldsymbol{\mathcal{U}} < 0 \\ 1, & \text{otherwise} \end{cases} \tag{2.24}$$

As noted by Springel (2010), this slope limiter is not total variation diminishing (TVD), so spurious oscillations can still occur near strong gradients. To counteract this, MANGA (optionally) applies an additional correction suggested by Duffell & MacFadyen (2011):

$$\langle\boldsymbol{\mathcal{U}}\rangle_i^{DM} = \boldsymbol{\alpha}_i^{DM}\langle\boldsymbol{\mathcal{U}}\rangle_i^{S10} \tag{2.25}$$

where $\boldsymbol{\alpha}_i^{DM} = \min(1, \psi'_{ij})$ and

$$\psi_{ij} = \begin{cases} \max[\theta(\boldsymbol{\mathcal{U}}_j - \boldsymbol{\mathcal{U}}_i)/\Delta\boldsymbol{\mathcal{U}}_{ij}, 1], & \text{for } \Delta\boldsymbol{\mathcal{U}}_{ij} > 0 \\ 1, & \text{otherwise} \end{cases} \tag{2.26}$$

where $\theta < 0.5$ gives a TVD limiter and $\theta = 1$ reduces it to the S10 slope limiter.

2.4.4 Velocities of Mesh-Generating Points

The hybridization of an ALE scheme allows it to act as a Eulerian scheme, a Lagrangian scheme or a combination of the both. For example, setting the mesh generating points' velocities to 0 ($\boldsymbol{w} = 0$) allows the code to behave as a static-mesh Eulerian scheme, while setting the velocities to $\boldsymbol{w} = \boldsymbol{v}$ allows the code to act as a Lagrangian scheme. While

MANGA applies the Lagrangian approach, it also applies corrections to $\boldsymbol{w}$ in the interest of keeping the Voronoi cells round, as suggested by Springel (2010). This avoids the problem of mesh tangling and distortions mentioned in Section 2.3. That is, the positions of the mesh-generating points $\boldsymbol{r}_i$ should be near to the centers of mass of the Voronoi cells c_i. To do this, MANGA corrects the velocity $\boldsymbol{w}_i$ such that it drifts toward the center at some fraction of the local sound speed $\chi c_{s,i}$. The mesh velocities are modified by:

$$\Delta \boldsymbol{w} = \chi c_{s,i} \frac{\boldsymbol{c}_i - \boldsymbol{r}_i}{d_i} \begin{cases} 0 & d_i < 0.9\zeta r_{\text{eff}} \\ \frac{d_i}{0.2\zeta r_{\text{eff}}} - 4.5 & 0.9\zeta r_{\text{eff}} \leq d_i \leq 1.1\zeta r_{\text{eff}} \\ 1 & d_i > 1.1\zeta r_{\text{eff}}, \end{cases} \tag{2.27}$$

where $d_i = |\boldsymbol{c}_i - \boldsymbol{r}_i|$, $c_{s,i}$ and $r_{\text{eff}} = (\frac{3}{4\pi}V_i)^{1/3}$ is the cell effective radius. We typically choose $\chi = 1$ and $\zeta = 0.25$ in our simulation runs.

2.4.5 Gravity Solver

The inclusion of (self-)gravity involves incorporating the gravitational potential into the momentum and energy equations. Following the suggestion of Springel (2010) for momentum:

$$\int_i \rho_i \boldsymbol{\nabla}\Phi_i dV = \frac{1}{2}\left(m_i^{(n)}\boldsymbol{\nabla}\Phi_i^{(n)} + m_i^{(n+1)}\boldsymbol{\nabla}\Phi_i^{(n+1)}\right) \tag{2.28}$$

And energy:

$$\int_i \rho_i \boldsymbol{\nabla} \Phi_i \cdot v \, dV = \frac{1}{2} m_i^{(n)} v_i^{(n)} \boldsymbol{\nabla} \Phi_i^{(n)} + \frac{1}{2} m_i^{(n+1)} v_i^{(n+1)} \boldsymbol{\nabla} \Phi_i^{(n+1)} \qquad (2.29)$$

The gradient of the gravitational potential, $\boldsymbol{\nabla}\Phi$ can either be user specified, derived from the solution of Poisson's equation:

$$\boldsymbol{\nabla}^2 \Phi = 4\pi G \rho \qquad (2.30)$$

for the case of self-gravity, or a hybrid of the two. For self-gravity, we use the tree-based solver in ChaNGa where each tree node contains the multipole mass moments up to hexadecapole order. The tree algorithm is based on PKDGrav as described in Stadel (2001). In this algorithm, the simulation domain is split into its eight octants, known as tree nodes. The mass multipole moments of each node are computed, and any node containing more than 12 particles is further split into its eight octants. This repeats until each leaf node of the tree contains 12 or less mesh generating points.

2.4.6 Other Modules

The original implementation of MANGA described by Chang et al. (2017) used an ideal, adiabatic equation of state (EOS). In Prust & Chang (2019), MANGA was extended to use the equations of state in MESA, an open-source stellar evolution code (Paxton et al., 2011, 2013, 2015). The MESA equation of state relies on several equations of state relevant over the different regimes of stellar structure. In the following sections, results will be from solely using the adiabatic EOS.

MANGA also includes multi-stepping to greatly improve the computational time for

simulations. Recently, modules have been added to MANGA to include physics such as Van Leer integration, radiative transfer (Chang et al., 2020), general relativistic hydrodynamics (GRHD) (Chang & Etienne, 2020), magnetohydrodynamics (MHD) (Spaulding, Chang Prust, in preparation) and nuclear burning (Humphrey Chang, submitted).

CHAPTER 3

Simulating Tidal Disruption Events

3.1 GENERATION OF INITIAL CONDITIONS

We construct initial conditions as follows. We first use a $1\ M_\odot$ star evolved with MESA (Paxton et al., 2011, 2013, 2015) from the pre-main sequence to the zero age main sequence. As in Prust & Chang (2019), we take the entropy profile and construct a star of mass M, whose entropy profile matches that of the original star.

In our numerical experiments, we start our stars at $r = r_0$ on a zero energy orbit with a periapse of $r_{\rm p}$. Thus, the initial magnitude of the velocity of the star is $v_0 = \sqrt{GM/r_0} = v_{\rm T}/\sqrt{\eta}$, where η is the ratio between r_0 and $r_{\rm T}$: $\eta = r_0/r_{\rm T}$.

We set $M_{\rm BH} = 10^6 M_\odot$, $M_* = 1 M_\odot$, and $R_* = 1\ R_\odot$, which gives $\alpha = 100$. We also use an adiabatic ideal gas ($\gamma = 5/3$) equation of state in these calculations, mainly for purposes of speed and its applicability at low densities. We set the initial distance to be $\eta = 10$.

3.2 SIMULATION SETUP

While the newly constructed star can contain a dark matter particle to model the core, which is done in common-envelope studies (Prust & Chang, 2019), we omit this feature in this study. This yields a radial profile of density and temperature that is then mapped to an unstructured particle (mesh generating point) mesh.

We construct an appropriate mesh for the star from a perturbed cubic distribution that has been periodically replicated to produce sufficient numbers of mesh-generating points. Such a cubic distribution approximates a cubic Eulerian grid, but the points are perturbed (slightly) so that we do not suffer from degenerate faces. We assume that each parti-

cle is representative of equal volumes, and we have rescaled their mass and temperature based on the appropriate radial position via the computed density $\rho(r)$ from MESA. These mesh-generating points are also endowed with a radially interpolated temperature. Outside of the star, we include a low density atmosphere of 10^{-15} g/cm^3 with temperature 10^5 K that extends out to the total box size of $5000 R_\odot$, having periodic boundary conditions at its edges. The periodic boundary conditions are currently the only boundary conditions that are implemented for hydrodynamics in MANGA. Other boundary conditions such as inflow or outflow boundary conditions are available for radiation (Chang et al., 2020). To lower the computational cost, we follow the methodology of Prust & Chang (2019) and use a mesh refinement algorithm to decrease the number of mesh-generating points in the atmosphere far from the star. We define a scale factor $\mathcal{S}(r) = (r/R_*)^n$ where R_* is the radius of the star, r is the spherical radius, and n is an adjustable parameter which we have set to $n = 2/3$ in this case. Starting with the same uniform replicated cubic distribution as for the star, the linear spacing between mesh-generating points is increased by $\mathcal{S}$ and their mass is increased by $\mathcal{S}^3$, preserving the external density. The resulting total number of mesh-generating points is 6.9×10^5 and 2.7×10^6 for 10^5 and 4×10^5 mesh-generating points for the star, respectively. In spite of our scaling of the atmospheric mesh, the majority of these points are still used to represent the low density atmosphere. We model the SMBH as a dark matter particle with a softened gravitational length of 6.14×10^{11} centimeters.

We check that the profiles produced from the mapping from 1-D stellar evolution codes to fully 3-D hydrodynamics simulations are in reasonable hydrostatic balance both for static Newtonian stars and boosted (moving, Newtonian) stars. In particular, we run these stars for a few dynamical times to check for stability of the profile. While it is not expected to be in perfect hydrostatic balance due to discretization errors, these stars do
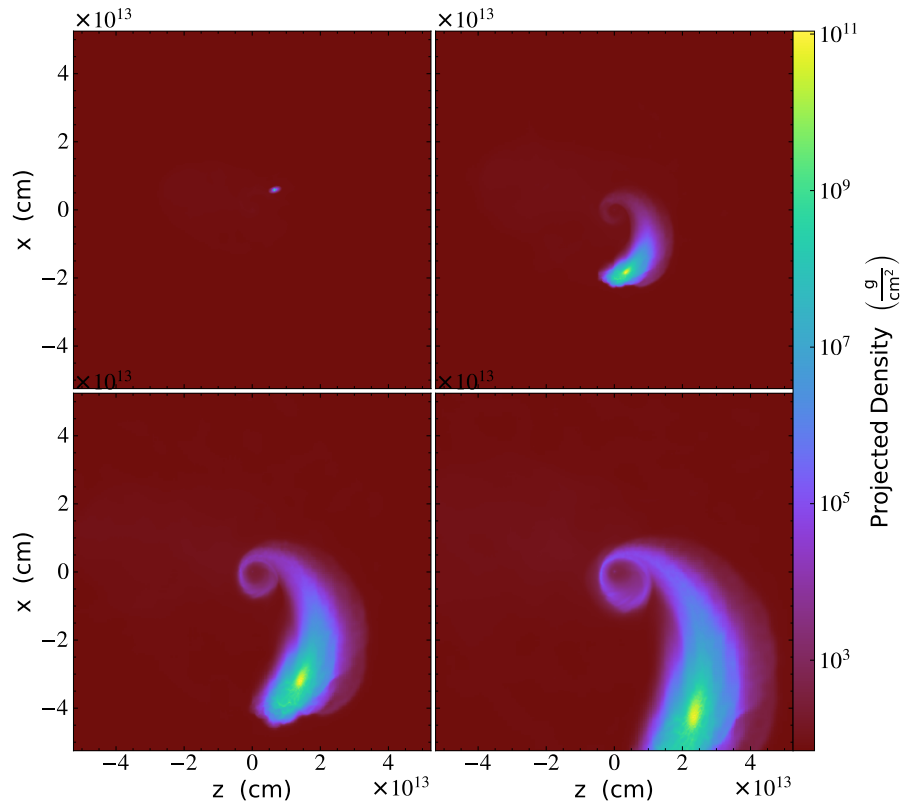
Figure 3.1: Projected density of a 1 $M_\odot$ star undergoing tidal disruption is shown from formation to 9 hours after the encounter with the black hole for $\beta = 2$. Each frame is 1.8 hours apart.

not oscillate significantly.

3.3 RESULTS

3.3.1 Energy Distribution

We vary β between 1 and 15 in our simulations to examine the effect of the impact parameter. This parameter study is similar to previous work by Guillochon & Ramirez-Ruiz (2013), but here we use a realistic star as opposed to a polytrope and use a MM code as opposed to the Eulerian grid code, FLASH (Fryxell et al., 2000). We use 10^5 mesh-generating
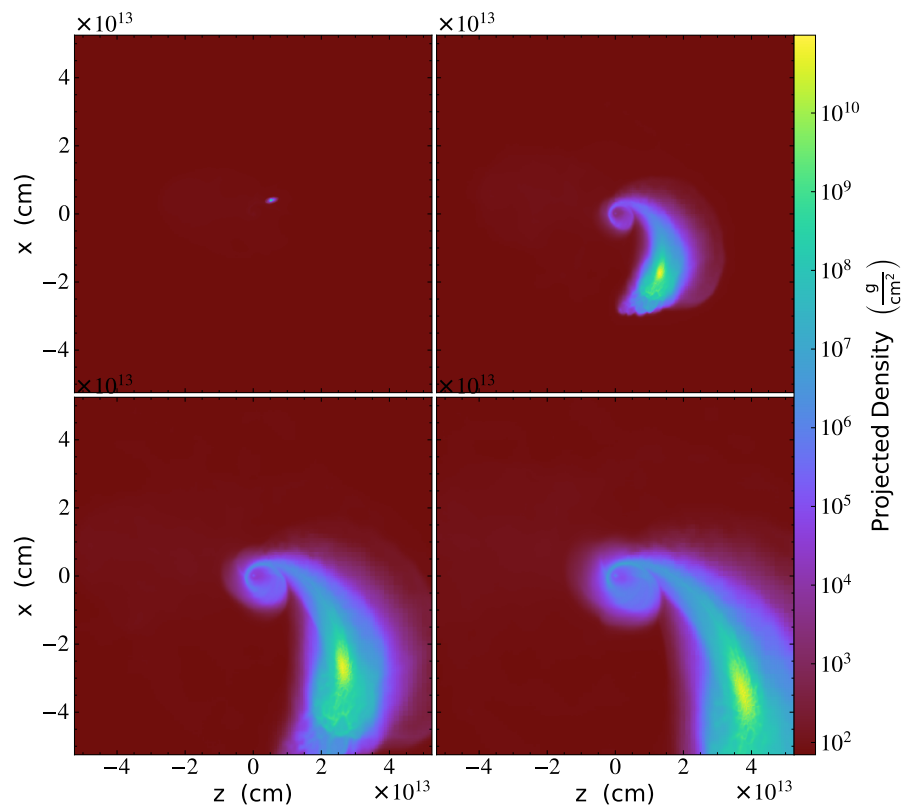
Figure 3.2: The disruption of a star with $\beta = 4$ is shown from formation to approximately 9 hours after the encounter. Each frame is 1.8 hours apart.

points to resolve the star for the parameter study, but confirm our result with two higher resolution studies at 4×10^5 mesh-generating points. These high resolution simulations are visualized in Figures 3.1 and 3.2 for $\beta = 2$ and 4, respectively. Here we show a sequence of images for the encounter for $\beta = 2$ (Fig. 3.1) and $\beta = 4$ (Fig. 3.2). The frames are at 3.6, 5.2, 6, and 7.8 hours from the start of the run. The two figures show the that fallback of material appears to be much more vigorous for larger β, e.g., closer approach. We also note that our focus is for star undergoing total disruption, which implies $\beta \gtrsim 2$ for a 1 $M_\odot$ star (Phinney, 1989; Guillochon & Ramirez-Ruiz, 2013; Mainetti et al., 2017; Ryu et al., 2020).

We have run simulations with β varying between 1-15. However, the optimistic upper limit is $\beta = 8$ for our calculation to be valid. In particular, we assume a Newtonian potential, but black holes are relativistic objects. The BH gravitational (Schwarzchild) radius is

$$r_g = \frac{2GM_{\mathrm{BH}}}{c^2} = 2.96 \times 10^{11} \left(\frac{M_{\mathrm{BH}}}{10^6 M_\odot} \right) \ \mathrm{cm} \tag{3.1}$$

This corresponds to a $\beta_g = \beta(R_g) = 23.5(M_{\mathrm{BH}}/10^6 M_\odot)^{-1}\alpha$. The relativistic corrections only decline (relatively) slowly with radius, e.g., the corrections decline like r_g/r. We must then choose β such that $\beta \ll \beta_g$. We take an optimist's view and noting that the innermost stable circular orbit is at $r_{\mathrm{ISCO}} = 3r_g$ and set an optimistic upper limit of β close to $\beta(r_{\mathrm{ISCO}}) \approx 8$. Hence the results for $\beta > 8$ are for the purposes of exploring parameter space, but are not reflective of the physics.

To understand how the fallback might vary as a function of β, we begin with the fallback rate of the debris, which is derived from Kepler's third law (Goicovic et al., 2019):

$$\dot{M} = \frac{dM}{dE}\frac{dE}{dt} = \frac{(2\pi GM_{\mathrm{BH}})^{2/3}}{3}\frac{dM}{dE}t^{-5/3}. \tag{3.2}$$
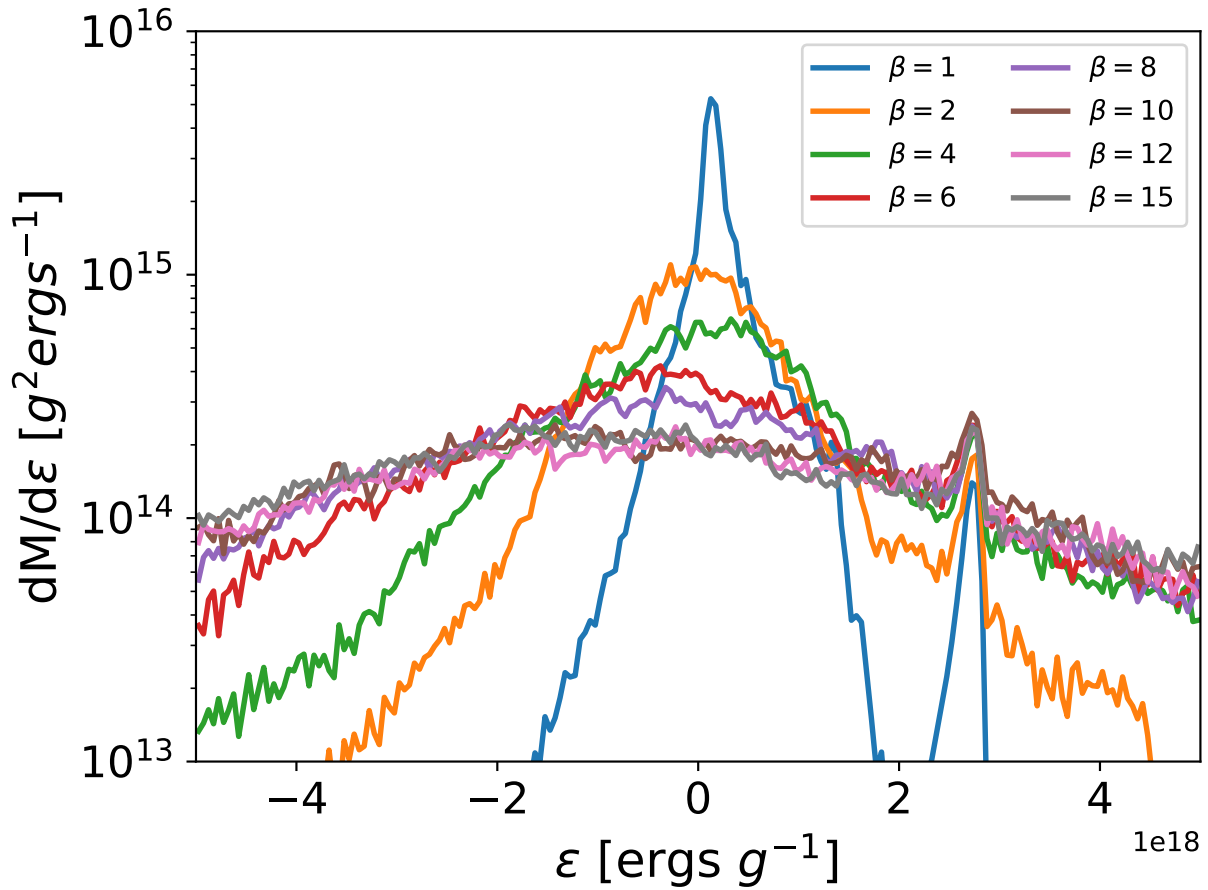
Figure 3.3: The mass as a function of specific energy for the $\beta = 1 - 15$. We can see the spread in energy increases with increasing β up to ~ 10. Above this value, the curve stops evolving.

Table 3.1: Energy spread σ is shown for each β value. Our simulations show a greater jump from $\beta=1$ to higher values than previously thought.

β	$\sigma/10^{18}$	β	$\sigma/10^{18}$
1	0.52	7	2.22
2	1.12	8	2.24
3	1.47	9	2.42
4	1.66	10	2.45
5	1.91	12	2.47
6	2.08	15	2.49

From the above equation, the fallback rate is related to the distribution of energy in the material. Thus, we plot the distribution of mechanical energy in Figure 3.3. It is immediately obvious that, ignoring the peak for $\beta = 1$, the spread of distribution of energy increases with increasing β. To quantify this spread, we fit the energy peak with a Gaussian of the form

$$\frac{dM}{dE} = \frac{M_0}{\sigma} \exp\left(-\frac{(E - E_0)^2}{2\sigma^2}\right) \tag{3.3}$$

where M_0, E_0, and σ are constants. We choose a Gaussian as it gives a reasonable fit over the region in energy space that contains the bulk of the mass. Here, σ provides an estimate of the energy spread, which we list in Table 3.1. We plot σ as a function of β in Figure 3.4 and find that it is well fit by a $\beta^{1/2}$ power law for $\beta = 2 - 9$. We will discuss the origin of this power-law relation below. For $\beta \gtrsim 10$, the energy spread, σ, flattens, and shows a clear transition to the "frozen-in" approximation as discussed in Stone et al. (2013).

3.3.2 Observational Effects

We now use equation (3.2) to compute the fallback rate onto the black hole as a function of time and plot the result in Figure 5.5. A few points are immediately noteworthy. On long timescales, $\dot{M}$ follows the theoretical fallback rate of $t^{-5/3}$ for the debris from the

Figure 3.4: β values are graphed with their corresponding σ values. We can see a relation of $\sigma \propto \beta^{1/2}$ with the dotted line. For $\beta \gtrsim 10$, it transitions to the frozen-in approximation.

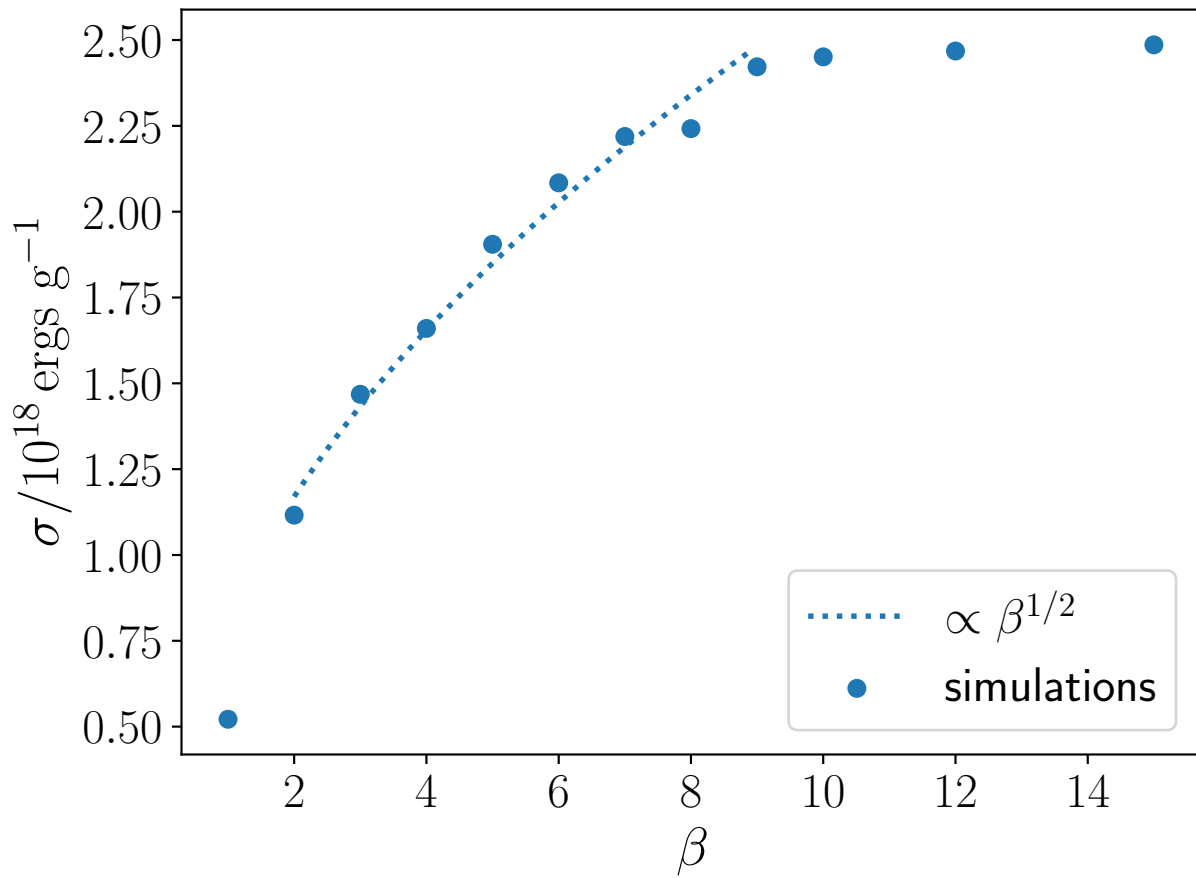star. This follows from the fact that dM/dE approaches a constant value near it peaks (by definition). Each $\beta \lesssim 10$ has a different peak luminosity time, which is about 2-4 months after the star's encounter with the SMBH. As β is increased, the peak time is shown to slightly shift earlier. For $\beta \gtrsim 10$, the "frozen-in" approximation implies that the evolution of $\dot{M}$ is fixed.

To find the peak time, we found the maximum $\dot{M}$ value from Figure 5.5 and then calculate the corresponding time. In Figure 3.6 we show the relationship between peak luminosity time and β. Here we find that t_{peak} is progressively earlier for increasing β up to ≈ 10. The earlier t_{peak} is in line with our previous result that the spread in dM/dE scales like $\beta^{1/2}$ for $\beta \lesssim 10$.

We also plot in Figure 3.6 the best fit normalization of the t_{peak} - β relation to the power law $\beta^{-3/4}$. We selected the power law based on the analysis in equation (3.11) below. While the fit does follow the general trend, it is not as good as the previous $\beta^{1/2}$ power law fit to σ in Figure 3.4. We also found no relation between β values and the peak $\dot{M}$ values. Our results in Figure 5.5 show a (roughly) fixed peak $\dot{M}$ for $\beta \geq 2$.

The dependence of the peak time as a function of when the star is disrupted is difficult to pin down observationally. However, this does have implications for the light curve. In particular, if we assume that the mass accretion rate after the peak scales like

$$\dot{M}(t > t_{\mathrm{peak}}) = \dot{M}_{\mathrm{peak}} \left(\frac{t}{t_{\mathrm{peak}}} \right)^{-5/3}, \tag{3.4}$$

then the fact that $t_{\mathrm{peak}} \propto \beta^{-3/4}$ implies that

$$\frac{\dot{M}(t_{\mathrm{peak}} + \Delta t)}{\dot{M}_{\mathrm{peak}}} \propto \beta^{-5/4}. \tag{3.5}$$

where Δt is some time measured from t_{peak}. The time after t_{peak}, Δt, should be chosen
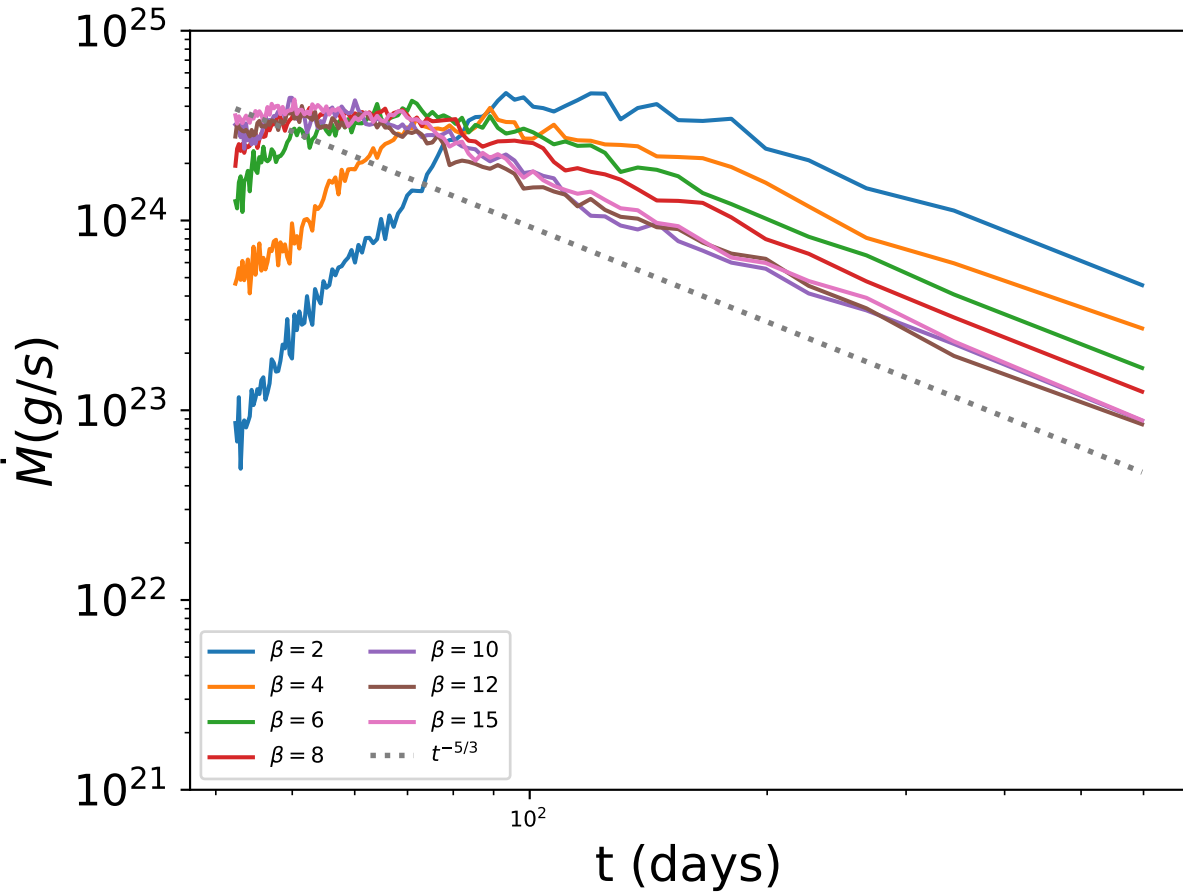
Figure 3.5: The fallback rate of the material into the black hole is shown to follow the theoretical rate of $t^{-5/3}$. $\beta \lesssim 10$ are shown to have slightly different peak times for the fallback rates. For $\beta \gtrsim 10$, the fallback rate stops evolving with β

.
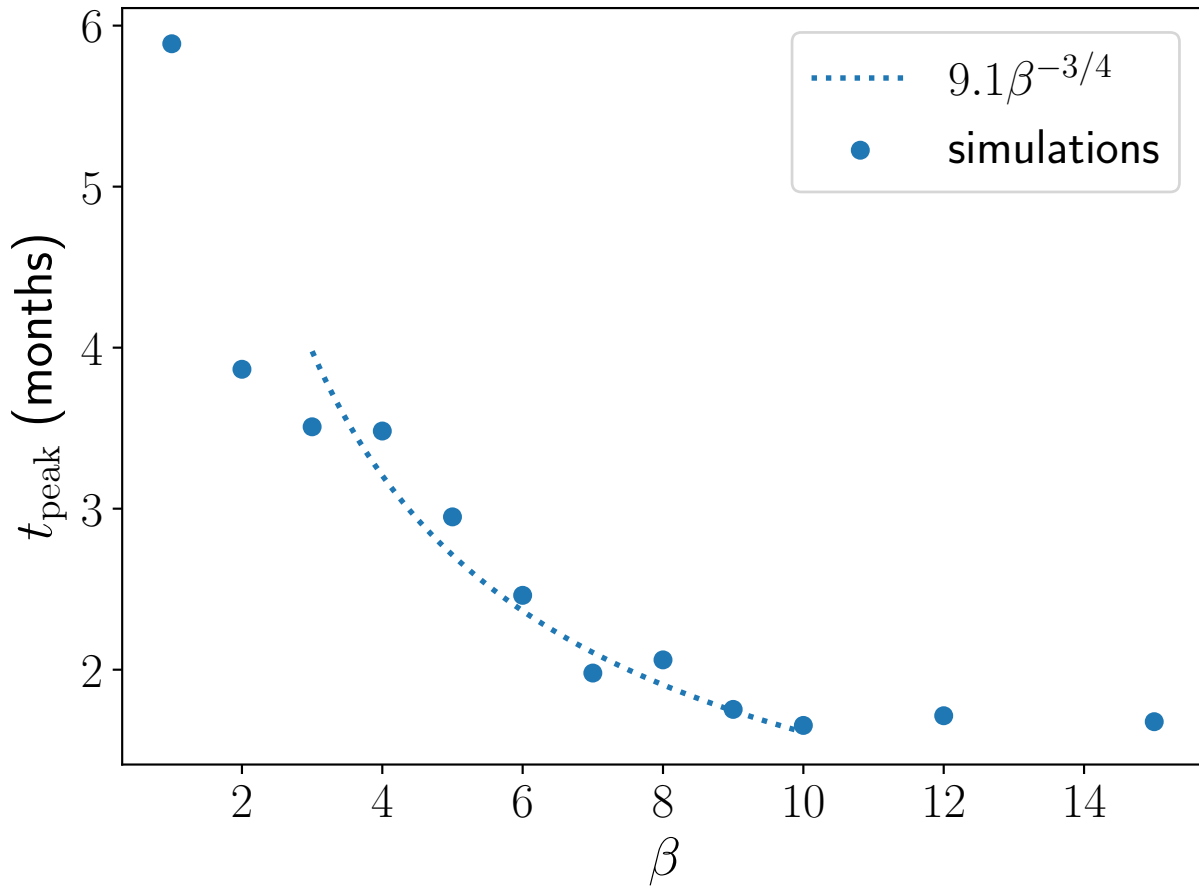
Figure 3.6: The peak time values corresponding to the peak fallback rate for beta values 1 through 15 are shown. The plot shows a dependence of $t_{\mathrm{peak}} \propto \beta^{-3/4}$ for $\beta \lesssim 10$. For $\beta \gtrsim 10$, this evolution stops, e.g., the "frozen-in" approximation.
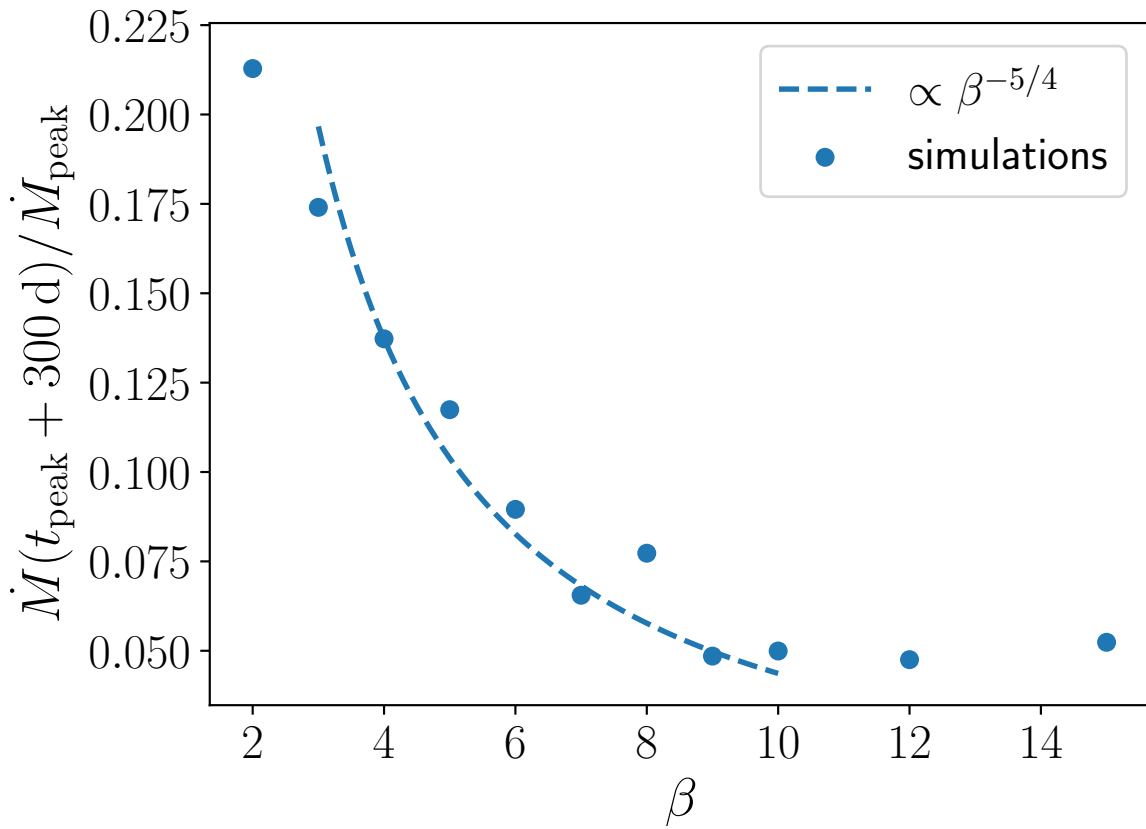
Figure 3.7: The fractional change of $\dot{M}$ relative to $\dot{M}_{\mathrm{peak}}$ is shown for β values 1 through 15. The Δt value is chosen to be 300 d. The dashed line shows a dependence of $\dot{M}(t_{\mathrm{peak}} + \Delta t)/\dot{M}_{\mathrm{peak}} \propto \beta^{-5/4}$.

so that $\Delta t \gg t_{\text{peak}}$. In Figure 3.7, we plot the fractional change in $\dot{M}$ relative to $\dot{M}_{\text{peak}}$ for $\Delta t = 300$ d.

The dependence of dM/dE on β is not entirely clear. Previous analytical (Stone et al., 2013) and numerical (Steinberg et al., 2019) studies have argued that dM/dE should follow the frozen-in approximation, e.g., no dependence on β, for large β's, though some allowance for a variation exists at small β. We find that the frozen in approximation holds for $\beta \gtrsim 10$. On the other hand, if we assume that the star stays intact to pericenter (see for instance Rees 1988; Ulmer 1999), we find a β^2 scaling. However, we see that this is clearly not the case for $\beta \lesssim 10$ shown in Figure 3.4 where the spread in energy is consistent with a $\beta^{1/2}$ scaling. This gives a factor of 2 variation over a small dynamic range.

To explain this scaling, we use the impulse approximation. We can approximate the star to be on a straight line orbit when it crosses the SMBH. When we expand the kinetic energy in a Taylor series, we will get the relationship that $\Delta v \propto \sigma$.

Starting with our definition of impulse:

$$\Delta p = \int F dt = \int F \frac{dt}{dr} dr \tag{3.6}$$

Substituting our tidal force from the SMBH:

$$F_{tidal} = \frac{GM_{BH}R_*}{r_p^3} \tag{3.7}$$

We arrive at:

$$\Delta p = \frac{GM_{BH}R_*}{r_p^2 v} \tag{3.8}$$

Which gives us a naive scaling of $\Delta v \propto \beta^{3/2}$ or $\sigma \propto \beta^{3/2}$, if we set $\Delta R = R_*$.

However, the star will not be fixed in size, e.q., hydrostatic equilibrium during this motion. Instead let us assume that the star is subject to both compressive and disruptive tidal forces. Here, we focus on the compressive forces. As the star is compressed by tidal gravity, we can assume it is resisted by gas/radiation pressure forces in the star. In virial equilibrium, we can estimate the central pressure by

$$P_c \sim \frac{GM_*^2}{R_*^4} \tag{3.9}$$

Multiplying by R_*^2 gives the force, which is exactly the self gravitation forces GM_*^2/R_*^2. Now instead if we replace the self-gravity by the (compressive) tidal force for the "compressed" star of radius R_*', we have

$$\frac{GM_*^2}{R_*'^2} = \frac{GM_{BH}M_*}{r_p^3}R_*' \rightarrow R_*' = \frac{R_*}{\beta} \tag{3.10}$$

In other words, the star is compressed by a factor of β at pericenter.

By setting $\Delta R = R_*'$ in our approximation, we will arrive at the result we found in our data of $\sigma \propto \beta^{1/2}$.

We note that this result differs significantly from results that assume that the star stays intact to pericenter (see for instance Rees 1988; Ulmer 1999), which will find a β^2 scaling, or assume that the fluid elements of the star follow purely ballistic trajectories, which gives no β scaling.

If we take the mild scaling of the energy spread for $\beta \approx 2-9$ as empirical, we show two important implications. First, let us consider the effect of this on the peak of the accretion

rate. Returning to equation (3.2), we maximize $\dot{M}$. Setting dM/dE to the Gaussian in equation (3.2) and noting that $E \propto t^{-2/3}$, we find (ignoring numerical factors):

$$\ddot{M} = 0 \propto 2\sigma^{-2}t^{4/3} - 5 \rightarrow t_{\mathrm{peak}} \propto \sigma^{-3/2} \propto \beta^{-3/4}, \tag{3.11}$$

using the previous scaling, $\sigma \propto \beta^{1/2}$. This turns out to be a reasonable fit to the behavior of the t_{peak} in Figure 3.6 for $\beta > 2$ as shown by the dashed line. Second, this leads to a variation in the change in the accretion rate (and hence luminosity) at a fixed time after the peak as shown in equation (3.5) above.

3.4 DISCUSSION AND CONCLUSIONS

In this paper, we studied the properties of the fallback rate as a function of β. By conducting a parameter study of β for a 1 $M_\odot$ star and a $10^6 M_\odot$ SMBH, we find that the spread in energy of the debris scales like $\beta^{1/2}$. This is important because the fallback rate of the material into the black hole is directly related to dM/dE. We also find that this results in an earlier t_{peak} for larger β.

Previous analytical work suggests either a β^2 dependence or no dependence of β, e.g., the "frozen-in" approximation. We find a slow $\beta^{1/2}$ evolution in dM/dE for $\beta \lesssim 10$, but recover the "frozen-in" approximation for $\beta \gtrsim 10$. We also present analytic arguments for both the scaling of dM/dE and t_{peak} with $\beta \lesssim 10$. We confirm convergence by running simulations varying the number of mesh-generating points that resolve the star from 10^5 to 4×10^5.

Guillochon & Ramirez-Ruiz (2013) found a similar but not exact match to our result in σ. While their work showed σ approaching a constant with higher β, our results still show some variation as beta increases that can be explained with the relation $\sigma \propto \beta^{1/2}$. This

relationship has not been mentioned in previous work. Guillochon & Ramirez-Ruiz (2013) also showed a result of t_{peak} decreasing with increasing β until $\beta = 2$, which our results support. However, our work shows t_{peak} to continue to decrease while they showed a slight increase in t_{peak} for $\beta > 2$. Higher β values seem to show a power law relation between peak luminosity time and β. It is still unclear how to relate this result to the theory. Similar to us, a fixed $\dot{M}$ was noted by Guillochon & Ramirez-Ruiz (2013) for $\beta \geq 2$.

Steinberg et al. (2019) focused on the evolution of the energy spread as a function of distance from the SMBH. They found overall the magnitude of the energy spread to be comparable with the frozen-in approximation, which predicts the energy spread to be independent of β, and that for $\beta=1$, the energy spread is larger than for the deeply penetrating cases. Our results show that the energy spread, $\sigma \propto \beta^{1/2}$, and the transition to the "frozen-in" approximation for larger β's. Finally, our work agrees with Goicovic et al. (2019)'s observation of the spread of energy in their simulations to be different than the frozen-in approximation.

As mentioned above, one cautionary note is that for the highest β values, relativistic corrections begin to become important. In particular, for $\beta = 8$, $r_p = 12.5\,R_\odot \approx 3r_g$, where $r_g = 2GM_{\mathrm{BH}}/c^2 = 4.2(M_{\mathrm{BH}}/10^6 M_\odot)R_\odot$. At these distances, relativistic effects will begin to affect the qualitative nature of these events, e.g., direct capture is a possibility. The transition to the "frozen-in" approximation occurs above this value raising the question of the relevance of this approximation for the system parameter studied in this problem. However, we should note that for $M_{\mathrm{BH}} \sim 10^5 M_\odot$, the ISCO is at $\beta \approx 37$, so that it is likely that the "frozen-in" approximation is recovered in this system.

By determining a relationship between observed TDE properties such as t_{peak}, we can get closer to inferring β for an observed TDE. Although our results show a fairly weak

relationship between t_{peak} and β, it is not weak observationally. Our relationship shows differences of months in peak luminosity time between β values, and this is a measurement we can clearly make using observations. After measuring t_{peak} we can figure out the evolution of $\dot{M}$, and this gives us two constraints on the same piece of information. From $\dot{M}$, we can infer stellar mass. If we take a main sequence star we know that the stellar structure does not change significantly, and with these pieces of information we can infer the β value of an observed TDE.

Observational searches for tidal disruption events have generally taken two paths, studies looking for X-ray transients and optical searches for supernova-like events (Maguire et al., 2020). Modeling work such as Mummery & Balbus (2020) could benefit from our results. By modeling the extremely luminous transient ASASSN-15lh, they showed that a relativistic thin disc model represents the TDE observations well. However, they use a ad-hoc source term in mass that is Gaussian in time. More sophisticated mass inflows from simulations such as ours can help put mutual constraint on both the mass inflow to periapse and the emission model.

Hinkle et al. (2020) showed that more luminous TDEs fade more slowly, but within each luminosity, there exists a bit of scatter in the rate of decline. Our results may help explain some of this scatter as we find that for the same events, the penetration parameter, β, can give a later peak and hence a broader peak. Our work could also improve studies such as these in determining impact parameter. For instance, long followup campaigns such as the work of Holoien et al. (2020) on the TDE event ASASSN-18pg, can use the fading luminosity to constrain β.

Care must be taken with applying these results to observations directly. First, additional physics such as black hole spin can significantly perturb the orbital trajectories of the disrupted stars and shift in time when the first self intersection of the debris may occur

(Guillochon & Ramirez-Ruiz, 2015; Stone et al., 2019; Gafton & Rosswog, 2019). Second, while the mass flow rate back to pericenter can be computed, converting this to an observed luminosity is not trivial. In particular, it remains an open question if accretion or shocks (see for instance Piran et al. 2015; Shiokawa et al. 2015; Lu & Bonnerot 2020) are responsible for the majority of the emission. Moreover, it is likely that outflow from disk formation or accretion changes the properties of the observed emission (Miller, 2015; Dai et al., 2018; Piro & Lu, 2020).

Constraints on the distribution of β would present an interesting probe of the dynamics near the center of galaxies (Stone & Metzger, 2016). In particular, a flat distribution of β or more likely a flat distribution in initial angular momentum coupled with the measure rates of TDEs would suggest that the loss-cones are full. On the other hand, distributions that peak toward low β would suggest empty loss cones. In particular, Weissbein & Sari (2017) has argued that the probability of high β TDEs in an empty loss cone scales like β^{-1}. This would place constraints on the mass distribution in galactic centers, the degree of non-sphericity, and the general orbits of stars in the central regions (for a review see Stone et al. 2020).

Finally, we plan future studies where we will explore the effect of radiation on the TDE debris using a recently developed radiation hydrodynamics solver (Chang et al., 2020) for MANGA. It is expected that radiation plays a crucial role in the initial disruption (Guillochon et al., 2009; Yalinewich et al., 2019a), self-crossing (Jiang et al., 2016), and the final accretion disk (Jiang et al., 2019). With the radiation hydrodynamics solver, MANGA should be particularly well suited for some of these problems.

CHAPTER 4

Radio Emission from Tidal Disruption Events

4.1 OVERVIEW

Recently, TDEs have been detected in the radio and have been followed up with radio observations, as discussed in further detail in Section 4.2. Motivated by these recent detections, we ran simulations of TDEs with different impact parameters to model their expected radio emission and determine any connections between the characteristics of the TDE and their radio emission signatures. To model the radio emission, we used the proposed model of the unbound debris from the TDE interacting with the local medium, as discussed in Section 4.2. Below, we describe our emission model, expected radio emission from our simulations, and how we can use this to understand radio emission from observed TDEs.

4.2 RADIO EMISSION FROM UNBOUND MATERIAL

The unbound material from a TDE will collide with the interstellar medium around the SMBH, driving a forward shock in that material. A fraction of the energy of the forward shock, ϵ_e, will accelerate electrons and another fraction ϵ_B will generate magnetic fields. These accelerated electrons and magnetic fields will then generate radio synchrotron emission. The physics of radio synchrotron emission by this unbound material is the same as that of many other astrophysics shocks, e.g., radio supernova. Thus we follow much of that literature here (see for instance Chevalier, 1998). Following Pacholczyk (1970), we

have

$$I_\nu = S(\nu_1) J\left(\frac{\nu}{\nu_1}, \gamma\right), \tag{4.1}$$

$$S(\nu_1) = \frac{c_5}{c_6} \left(B \sin\theta\right)^{-1/2} \left(\frac{\nu_1}{2c_1}\right)^{5/2}, \tag{4.2}$$

$$J(z, \gamma) = z^{5/2} \left[1 - \exp\left(-z^{-(\gamma+4)/2}\right)\right] \tag{4.3}$$

where I_ν is the radiation intensity, B is the magnetic field, and parameters $c_5 = 7.52 \times 10^{-24}$ and $c_6 = 7.67 \times 10^{-41}$ are constants in cgs units calculated by Pacholczyk (1970). The asymptotic limits for $\nu \ll \nu_1$ and $\nu \gg \nu_1$ gives the respective power law scaling for optically thick and thin synchrotron emission, respectively. The frequency at which optically thin and thick emission transitions, ν_1, is

$$\nu_1 = 2c_1 (sc_6)^{2/7} N_0^{2/7} B^{5/7}, \tag{4.4}$$

where $c_1 = 6.27 \times 10^{18}$ in cgs units, s is the extent of the emission region, following Pacholczyk (1970), and N_0 is the normalization for the power-law distribution of relativistic electrons accelerated by the shock (Pacholczyk, 1970). This power law distribution of the relativistic electron density, n_r, is

$$\frac{dn_r}{dE}(> E) = N_0 E^{-\gamma} = \frac{n_{r,0}}{E_{\min}} \left(\frac{E}{E_{\min}}\right)^{-\gamma}, \tag{4.5}$$

where E is the electron's energy, $E_{\min}$ is the minimum energy of relativistically accelerated electrons, $n_{r,0}$ is the normalization, and $\gamma = 3$ is the power law index. We write the power-law distribution in two ways to link the formalism of Pacholczyk (1970) and a clearer formalism where the units of variables are more obvious.

Previously, Krolik et al. (2016) has taken these equations and derived both the peak

radio frequency and peak flux and we follow the same arguments here. We should also note that a follow-up result in Matsumoto et al. (2022) uses a more sophisticated estimate for the synchrotron radiation provided by Barniol Duran et al. (2013), but as we will see, the results are fairly similar. Integrating equation (4.5) from $E = E_{\min}$ to ∞, we find:

$$N_0 = n_{r,0}E_{\min}^{\gamma-1} = (\gamma - 1)E_{\min}^{\gamma-1}\zeta_e n, \tag{4.6}$$

where ζ_e is the fraction of electrons accelerated to relativistic energies and n is the local electron/proton density.

$$\frac{E_{\min}}{m_e c^2} = \frac{(\gamma - 2)\epsilon_e m_p v_s^2}{(\gamma - 1)\zeta_e m_e c^2} \approx \frac{\epsilon_{e,-1}}{\zeta_{e,-1}}v_{s,4}^2, \tag{4.7}$$

where $v_{s,4} = v_s/10^4\,\mathrm{km\,s^{-1}}$, $\epsilon_{e,-1} = \epsilon_e/0.1$, and $\zeta_{e,-1} = \zeta_e/0.1$. The magnetic field is then:

$$B = \sqrt{8\pi\epsilon_b m_p n v_s^2} = 0.2\epsilon_{b,-1}^{1/2}n_4^{1/2}v_{s,4}\,\mathrm{G} \tag{4.8}$$

where $n_4 = n/10^4\,\mathrm{cm^{-3}}$.

Finally assuming a constant speed shock $s = v_s t$ and the extent of the emission region equal to radius of the shock, equation (4.4) becomes

$$\nu_1 = 0.83\epsilon_{e,-1}^{4/7}\zeta_{e,-1}^{2/7}\epsilon_{b,-1}^{5/14}v_{s,4}^{11/7}n_4^{9/14}f_{0.15}^{2/7}t_{100}^{2/7}\,\mathrm{GHz}, \tag{4.9}$$

where $f_{0.15} = f/0.15$, f is the fraction of the sky which is subtended by the tidal debris, and $t_{100} = t/100\,\mathrm{d}$. The peak flux is then

$$F(\nu_1) = 2.5\pi v_s^2 t^2 f d^{-2}S(\nu_1) \tag{4.10}$$

where d is the distance to the source and the constant $2.5 = 4J(z = 1, \gamma)$ includes the correction for $J(z = 1, \gamma)$. We then have

$$F = 0.7 d_2^{-2} \epsilon_{e,-1}^{10/7} \zeta_{e,-1}^{5/7} \epsilon_{b,-1}^{9/14} f_{0.15}^{19/14} n_4^{19/14} v_{s,4}^{38/7} t_2^{19/7} \mu\text{Jy}, \tag{4.11}$$

where $d_2 = d/10^2 \, \text{Mpc}$.

4.3   NUMERICAL RESULTS

Equations (4.9) and (4.11) show that peak frequency and flux depends on the geometry and velocity of the ejecta, the external environment, and the microphysics of electron acceleration and magnetic field generation. To place a constraint on the geometry and velocity of the ejecta, we used numerical simulations of TDEs described previously in Spaulding & Chang (2021).

To summarize these simulations, we used the moving-mesh simulation code, MANGA(Chang et al., 2017; Prust & Chang, 2019), to conduct a parameter study of a 1 $M_\odot$ star encountering a $10^6 M_\odot$ SMBH with a penetration depth, $\beta = 1 - 15$. The penetration depth is parameterized by $\beta = r_t/r_p$, where r_p is the periapse, $r_t = (M_{\text{BH}}/M_*)^{1/3} R_*$ is the tidal radius, M_{BH} is the mass of the SMBH, M_* is the mass of the star, and R_* is the radius of the star. We used between $10^5 (6.9 \times 10^5)$ and $4 \times 10^5 (2.7 \times 10^6)$ mesh-generating points for the star (star and background). We model the SMBH as a dark matter particle with a softened gravitational length of 6.14×10^{11} cm. For this paper, we have also performed a $\beta = 1.5$ simulation. The interested reader is referred to Spaulding & Chang (2021) for more details.

In the previous Chapter 3, we showed that the width of the energy distribution scales like $\Delta E \propto \beta^{1/2}$. This scaling of the distribution of energy with the penetration depth also
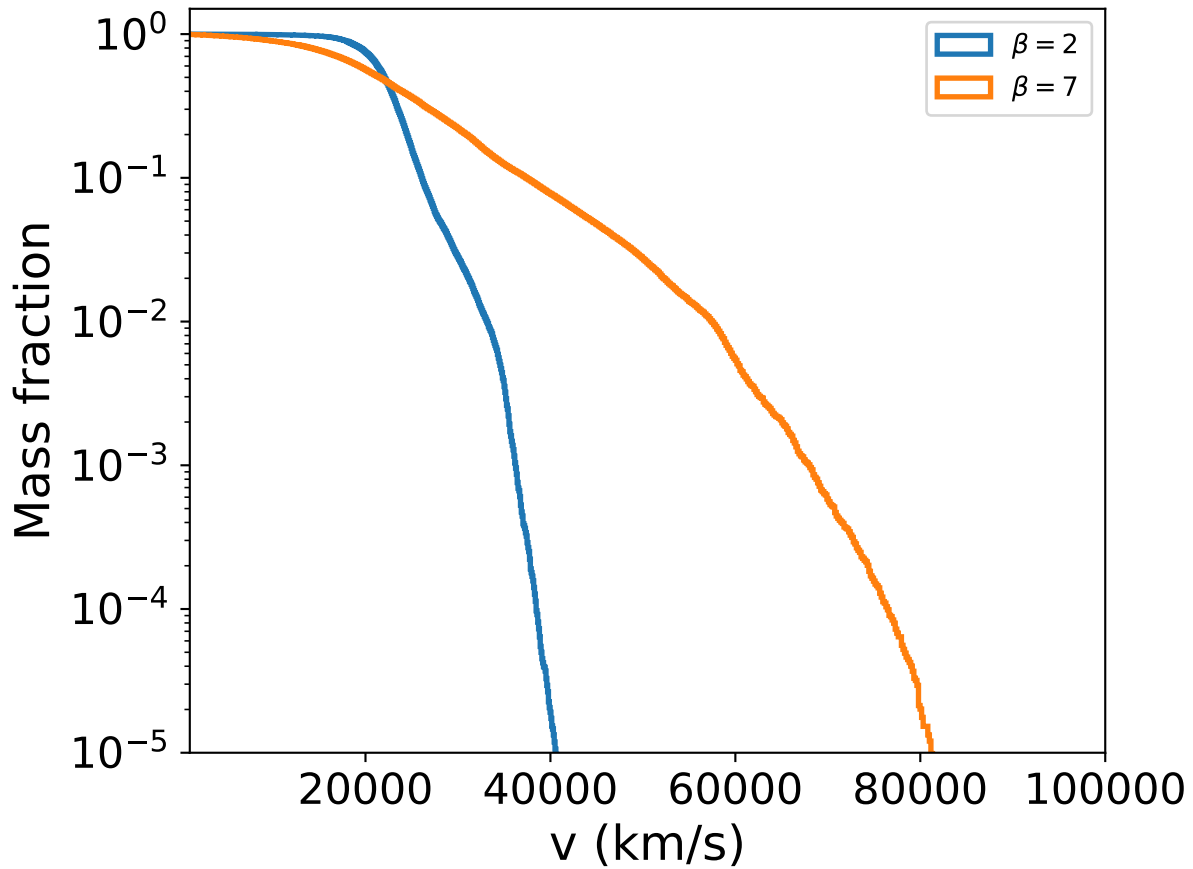
Figure 4.1: The cumulative distribution of the velocity of the unbound debris is shown for $\beta = 2$ and $\beta = 7$. The distribution of $\beta = 7$, the closer impact, shows a significant increase in velocity.
.

suggests that the velocity distribution of the unbound material should also scale with β. This is shown in Figure 4.1 where we show the reverse cumulative mass-fraction distribution function of v for $\beta = 2$ and $\beta = 7$. The reverse cumulative distribution of v shows a significantly larger tail of velocity extending for higher β value, e.g., closer approach. This is also seen qualitatively in similar moving-mesh simulations by Yalinewich et al. (2019b).

Setting the highest velocity, v_{max} to be defined as the velocity with a mass fraction

above 10^{-4}, we plot v_{max} as a function of β in Figure 4.2. Here it is evident that higher β values correspond to larger v_{max}. This is important because the flux, specifically the peak flux, is strongly dependent on velocity. A linear fit to this result gives:

$$v_r = (2.3 + 0.24\beta) \times 10^4\,\mathrm{km\,s^{-1}} \tag{4.12}$$

This relationship is valid for $\beta \leq 10$. For $\beta > 10$, we have previously shown that the distribution of energies follow the "frozen-in" approximation (Spaulding & Chang, 2021) and thus the energies and velocities asymptote.

We now turn to the geometry of the ejecta, focusing on the filling fraction of the sky that the unbound ejecta occupies. In Figure 4.3 we show the average velocity of unbound material with $v > 2 \times 10^4$ and $v > 4 \times 10^4\,\mathrm{km\,s^{-1}}$ for $\beta = 2$ and 7, respectively as a function of θ. As this plot shows, the distribution of velocity as a function of θ is fairly flat up to around 45 degrees. This gives us an opening angle of 90 degrees and thus we find $f = (4\pi)^{-1} \int d\Omega = (1/2) \int_0^{\pi/4} d\cos\theta \approx 0.15$. This value is consistent with the analytic estimates made by Krolik et al. (2016) of $f \approx 0.2$.

Using these highest velocities derived from our simulations as a function of β, we compute the radio spectrum for a number of β's using equations(4.1)-(4.8) and plot this in Figure 4.4 for $\beta = 1, 3, 5, 10$ and 15. We use the model parameters $\epsilon_{e,-1}$, $\epsilon_{b,-1}$, $f_{0.15}$, $\zeta_{e,-1}$, n_4, and t_2 to unity. The peak flux increases and shifts to higher frequency for larger βs, because of the associated higher velocities. This suggests that observed flux values could constrain the impact parameter, β, of the observed TDE. Moreover, observations over several epochs can constrain properties of the central regions of galaxies such as n_4 and the density profile as a function of radius.

To see how strongly the flux was impacted by higher velocities, we plot the peak flux for each β from our simulations in Figure 4.5. Using the fit found earlier (eq.[4.12]), we
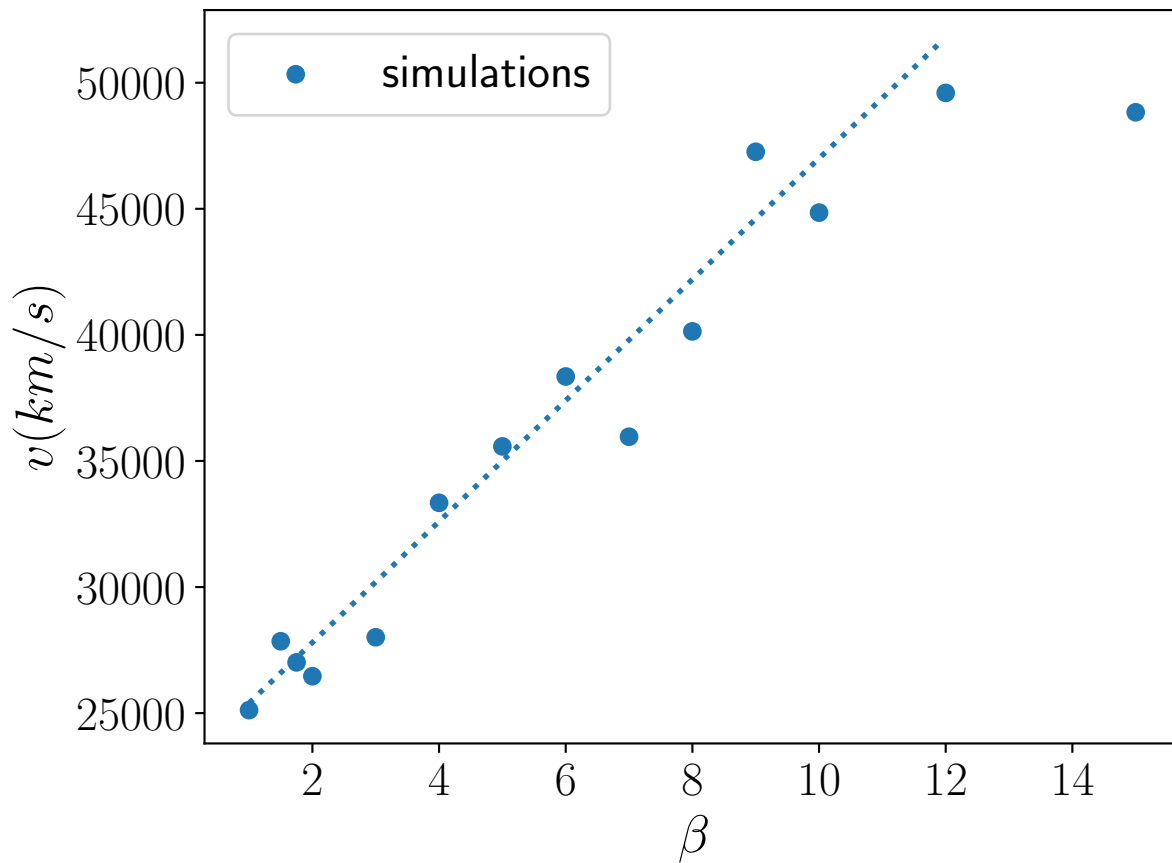
Figure 4.2: For β values of 1-12, the highest velocity of the unbound debris has a linear relationship to β. The fit goes as $v = (0.23 \times 10^9)\beta + 2.3 \times 10^9$ which is shown with the dotted line. This will result in different peak flux values for each β.
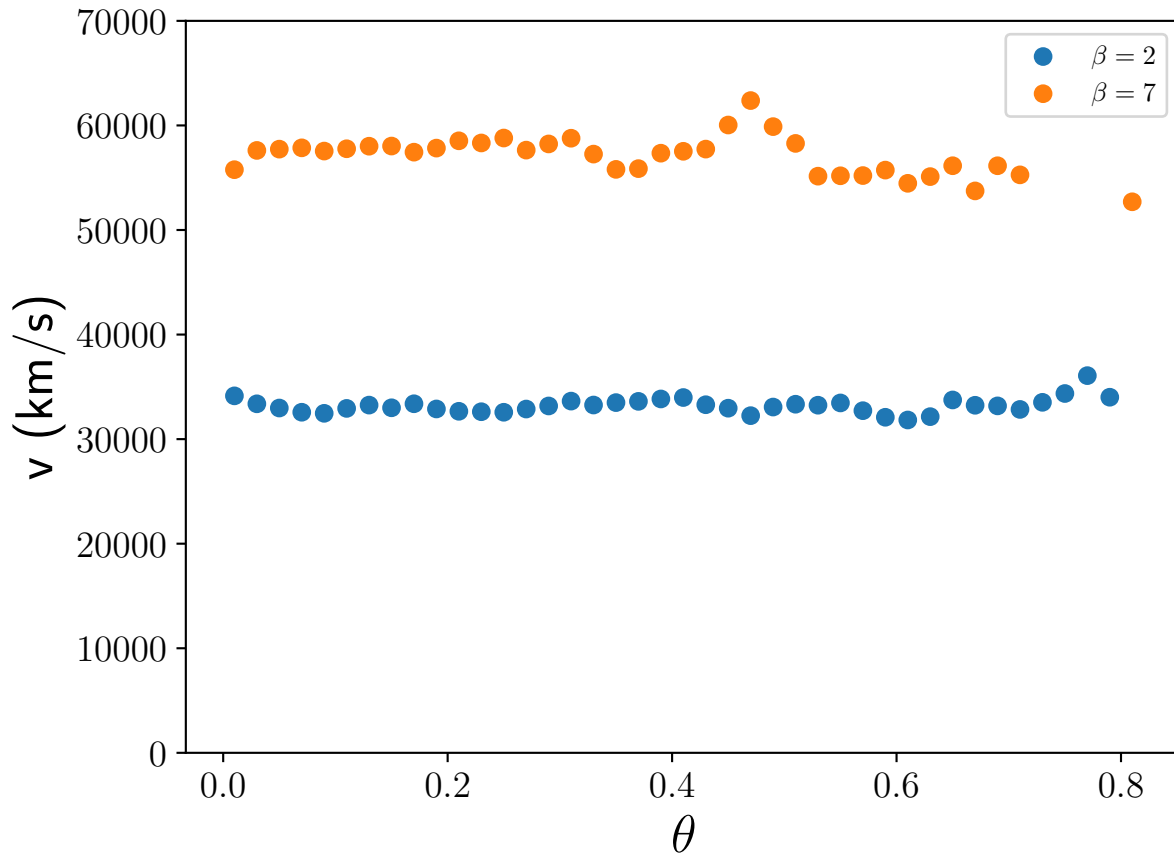
Figure 4.3: Average velocity of material with $v > 2 \times 10^4$ and $> 4 \times 10^4 \, \mathrm{km \, s^{-1}}$ for $\beta = 2$ and 7, respectively as a function of θ. This shows that distribution of the highest velocity material follows a rather flat distribution up to an opening angle of ≈ 45 degrees.
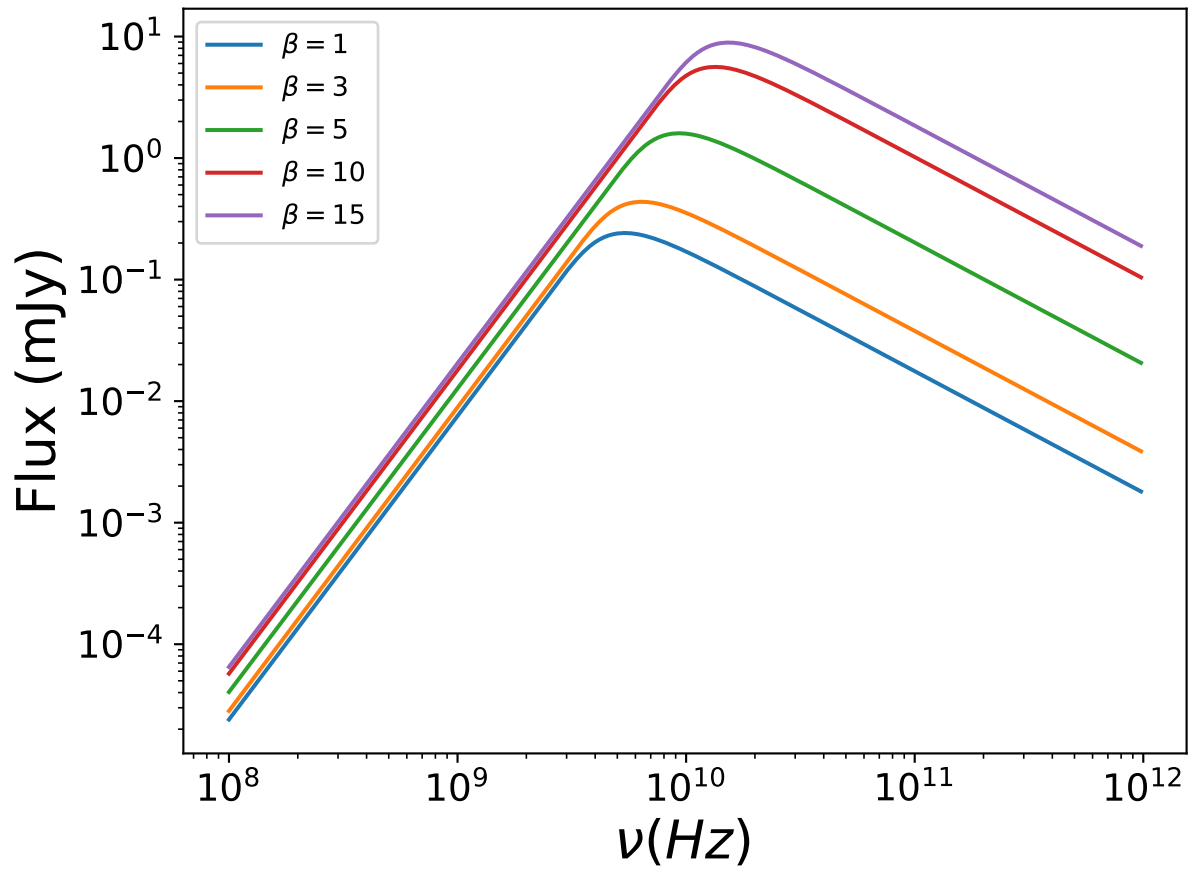
Figure 4.4: The magnitude of the flux is shown for β values 1,3,5,10,15. The peak flux values are shown to slightly increase for each β value, due to the corresponding increase in velocities.
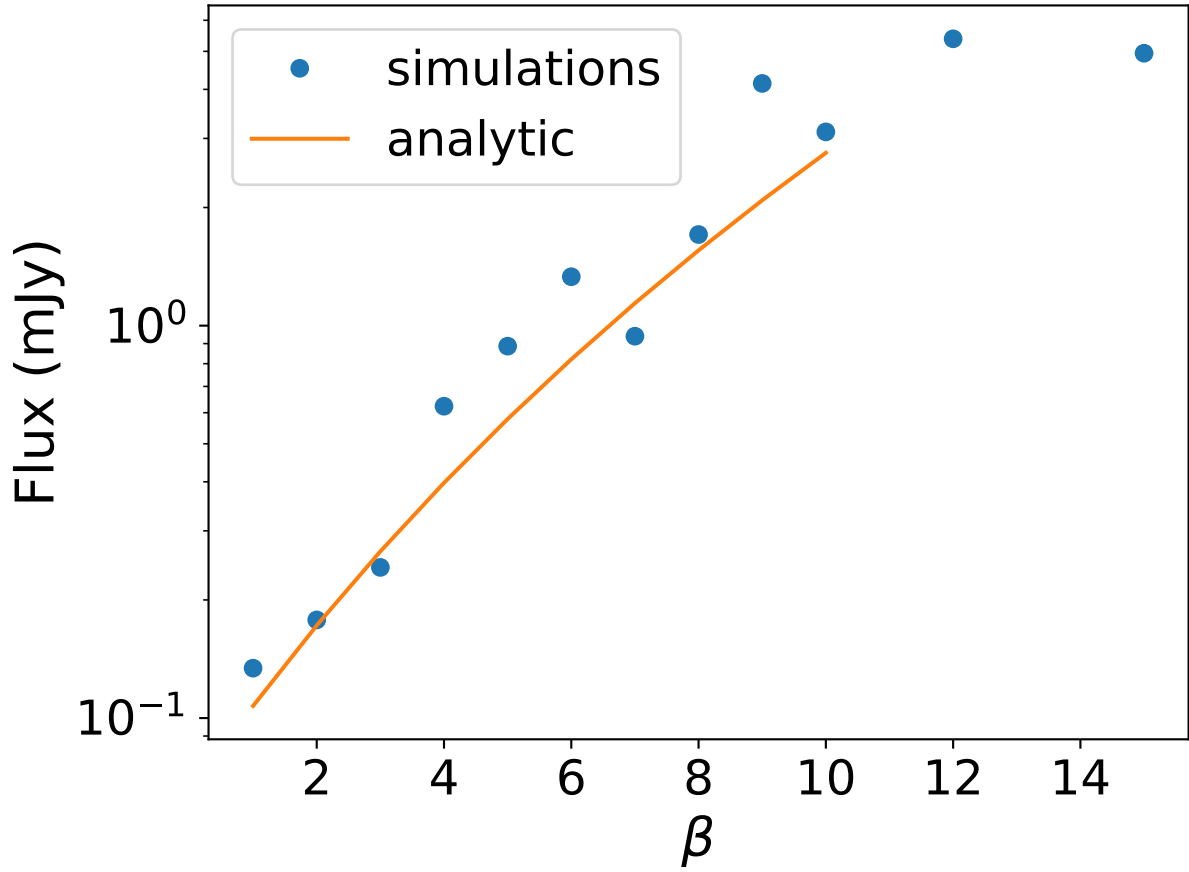
Figure 4.5: Peak flux as a function of β from simulations. We also overplot the peak flux from our analytic fit for the velocity as a function of β (eq (4.12)), which is a good match to the simulated values.

can compute an analytic fit for peak flux using the model parameters as stated above:

$$F = 64 d_2^{-2} \epsilon_{e,-1}^{10/7} \zeta_{e,-1}^{5/7} \epsilon_{b,-1}^{9/14} f_{0.15}^{19/14} n_4^{19/14} (1 + 0.1\beta)^{38/7} t_2^{19/7} \mu\text{Jy} \tag{4.13}$$

The analytic result is a good fit up to $\beta \approx 10$ as show in the solid line in Figure 4.5.

4.4 CONNECTING TO OBSERVATIONS

To connect our results to observations, we look at four TDEs that have observed radio emission summarized by Alexander et al. (2020), where the observed radio emission was attributed to a non-relativistic outflow and not to a relativistic jet. The four TDEs are AT2019dsg, CNSS J0019+00, ASASSN-14li, and XMMSL1 J0740-85. We obtain the observed peak flux and peak frequencies for each TDE from Stein et al. (2021) and Cendes et al. (2021), Anderson et al. (2020), Alexander et al. (2016), and Alexander et al. (2017), respectively, and collate them in Table 4.1.

AT2019dsg was discovered by ZTF on 2019 April 9 and was classified as a TDE on the basis of its optical spectrum with a measured redshift of z = 0.051, implying a luminosity distance of ≈ 230 Mpc. Radio observations were obtained from VLA, AMI, and MeerKAT at four epochs with times listed in Table 4.1 from Stein et al. (2021) and Cendes et al. (2021). Stein et al. (2021) applied a Markov chain Monte Carlo approach to determine the peak frequency, ν_1, and peak flux, F_{ν_1} of each epoch.

CNSS J0019+00 was first identified in the Caltech-NRAO Stripe82 Survey epoch 4 on 2015 March 21. It is located in the nucleus of a nearby (z = 0.018) galaxy Anderson et al. (2020). CNSS is a five-epoch survey with the NSF's Karl G. Jansky Very Large Array at S band (2–4 GHz) that was carried out between 2013 December and 2015 May. The spectra of CNSS J0019+00 was well described by synchrotron emission from an outflow expanding into and shocking the ambient medium.

On 2014 November 22, the All Sky Automated Survey for SuperNovae (ASAS-SN) reported the discovery of the new transient ASASSN-14li at a distance of 90 Mpc Alexander et al. (2016). Follow up radio observations were initiated using the Karl G. Jansky Very Large Array (VLA). Six epochs of observations were obtained between 2014 December 24 and 2015 September 11. Alexander et al. (2016) modelled the radio data with the

standard synchrotron emission model. The peak frequency and flux are derived from a synchrotron equipartition model.

On 2014 April 1, the XMM-Newton X-ray satelite detected a flare from the nucleus of the nearby (z = 0.0173, d = 75 Mpc) quiescent galaxy 2MASS 07400785-8539307 as part of the XMM-Newton slew survey. The position of XMMSL1 J0740-85 was then observed with the Australia Telescope Compact Array (ATCA) beginning on 2015 November 14, 592 days after the initial X-ray discovery Alexander et al. (2017). This resulted in four epochs of observations. Using a MCMC technique, the data was fit to find the peak frequency and flux.

As stated above, observations over multiple epochs combined with the distance can be used to determine the density profile of the centers of galaxies and velocity of the outflow for fixed ϵ_B, ϵ_e, ζ_e, and f. Our results for n and v using multi-epoch observations from each TDE are shown in Figure 4.6 and listed in Table 4.1. We fit a power law ($n \propto r^{-k}$) density profile[1], using the orthogonal distance regression routines built into the scipy package (Virtanen et al., 2020). The best-fit power-law index, k, for AT2019dsg (squares), ASASSN-14li (circles), and CNSS J0019+00 (diamonds), are 1.91 ± 0.20, 2.73 ± 0.11, and 2.61 ± 0.15, respectively, for a filling fraction of $f = 0.15$. The associated reduced χ^2's are 0.61, 0.46, and 0.84, respectively. Our motivation for the lower value of f follows from our simulations that suggest that the unbound material fills up about 15% of the sky. The last TDE, XMMSL1 J0740-85, only had one data point so this process is not possible.

Looking at Table 4.1, we note that the v's for each TDE remained nearly constant across epochs. Here we find that the velocities of ASASSN-14li, CNSS J0019+00, and XMMSL1 J0740-85 are similar to what we expect from our simulations for $\beta \approx 2$, e.g., velocities around $2 - 3 \times 10^4 \, \mathrm{km \, s^{-1}}$. AT2019dsg is a bit of an outlier here with significantly larger

---

[1]We should note that the ISM near the centers of galaxies are not necessarily a power law (see for instance, Quataert, 2004).

variance and overall velocities, though the velocities are still consistent with a deep penetration TDE, e.g., $\beta \sim 10$. As a point of comparison, we also plot the results of Matsumoto et al. (2022) for AT2019dsg (triangles) in Figure 4.6. Here, we find that our power law fit gives the same index within errors, but that the radial extent is larger in our estimate than theirs. While it is the case that we are using a less sophisticated analysis for the synchrotron estimate than Matsumoto et al. (2022), we are also using somewhat different parameters. In particular, Matsumoto et al. (2022) uses $f = 0.36$, which is a more spherical outflow, $f \sim 1$. This drops the velocity to be more in line with the expectations the other two TDEs, though it is not clear if this is a relevant expectation.

We note some caution with these results as they depend strongly on parameters such as ϵ_b, ϵ_e, ζ_e, and f, which are not well constrained. For lower values of these parameters, the associated v would increase, lowering n. We also note that the variation in velocity of the outflow varies by about 10-20% at most across epochs except for AT2019dsg. The fact that the velocity does not vary tremendously is in line with a freely expanding shell on ballistic trajectories. This is not surprising because at the fitted density, fitted velocity, and time of observation, the total mass swept up in a shell is:

$$M_{\mathrm{sh}} = \frac{4\pi}{3} m_p n r_{\mathrm{sh}}^3 \approx 5 \times 10^{-6} n_4 v_{s,4}^3 t_2^3 M_\odot, \tag{4.14}$$

where $r_{\mathrm{sh}} = v_s t$ is the radius of the shell. The mass of the shell is much smaller than the mass of the highest velocity material and so we do not expect that highest velocity unbound material to be significantly slowed.
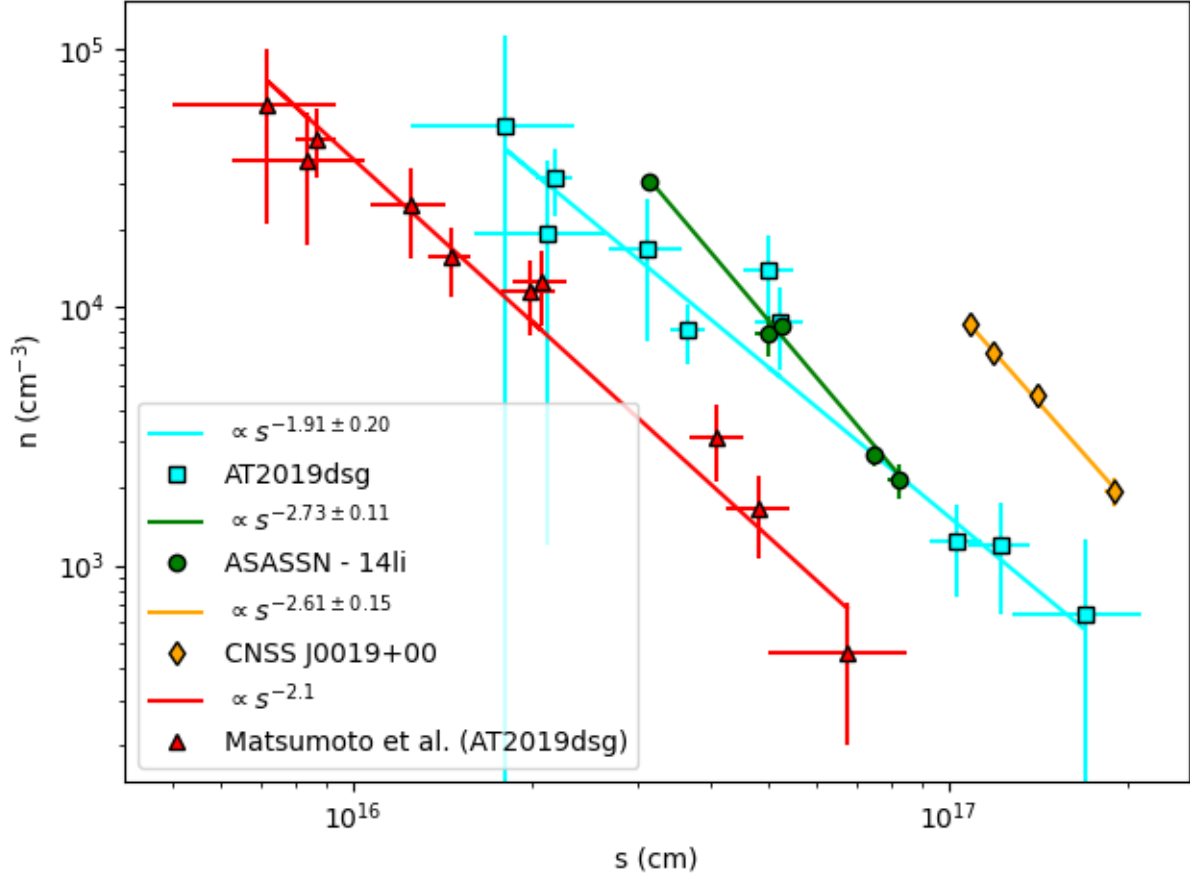
Figure 4.6: The density profile of $n \propto s^{-k}$ can be constrained using the radio TDE observations of ν_1 and F. The density (n) and velocity of the unbound debris (v) are found from equitation analysis of Equations 4.9 and 4.11 and the radius of the outflow is approximated by $s \approx vt$. The best-fit power-law index, k, for AT2019dsg, ASASSN-14li, and CNSS J0019+00, are 1.91 ± 0.20, 2.73 ± 0.11, and 2.61 ± 0.15, respectively, for a filling fraction of $f = 0.15$. The associated reduced χ^2's are 0.61, 0.46, and 0.84, respectively. We compare AT2019dsg to work done by Matsumoto et al. (2022). Our $k = 1.91$ value is in close agreement to Matsumoto et al. (2022) who found a fit of $k = 2.1$.

Table 4.1: We looked at four TDEs with radio emission that is proposed to develop from the outflow. Using equations 4.9 and 4.11 and observational results of ν_1 and flux, we computed the velocity of the outflow and the density of the ambient medium (n) for an opening angle of f = 0.15. We constrained the density profile parameter, k, fitting $n \propto s^{-k}$ as shown in figure 4.6. We could not fit a k value for XMMSLI J0740-85 because of insufficient number of data points.

Name	d(Mpc)	fitted k	t(days)	ν_1(GHz)	F_ν(mJy)	s (cm) $\times 10^{16}$	n (cm^{-3}) $\times 10^3$	v(km/s) $\times 10^3$
$f = 0.15$								
AT2019dsg	230	1.91 ± 0.20	42	15.8 ± 3.6	0.47 ± 0.09	2.1 ± 0.5	19 ± 17	58 ± 14
			45	20.9 ± 6.3	0.60 ± 0.04	1.8 ± 0.5	51 ± 61	46 ± 14
			50	18.2 ± 1.3	0.67 ± 0.01	2.2 ± 0.2	32 ± 9.0	50 ± 3.6
			70	13.8 ± 1.9	0.80 ± 0.06	3.1 ± 0.4	17 ± 9.3	52 ± 7.3
			72	10.7 ± 0.7	0.65 ± 0.03	3.6 ± 0.2	8.1 ± 2.2	59 ± 4.0
			120	10.2 ± 0.9	1.24 ± 0.05	5.2 ± 0.5	8.8 ± 3.1	50 ± 4.5
			151	9.5 ± 0.9	0.98 ± 0.04	5.0 ± 0.5	14 ± 5.3	38 ± 3.7
			178	5.1 ± 0.5	1.22 ± 0.04	10 ± 1.0	1.2 ± 0.4	67 ± 6.7
			290	3.5 ± 0.4	0.79 ± 0.04	12 ± 1.4	1.2 ± 0.5	49 ± 5.7
			551	1.7 ± 0.4	0.34 ± 0.04	17 ± 4.1	0.6 ± 0.6	35 ± 8.6
ASASSN - 14li	90	2.73 ± 0.11	143	8.2 ± 0.10	1.76 ± 0.01	3.1 ± 0.04	31 ± 1.5	25 ± 0.3
			207	4.37 ± 0.20	1.23 ± 0.03	5.0 ± 0.2	7.8 ± 1.4	27 ± 1.3
			246	4 ± 0.06	1.14 ± 0.01	5.2 ± 0.09	8.5 ± 0.5	25 ± 0.3
			304	2.55 ± 0.06	0.94 ± 0.02	7.5 ± 0.2	2.7 ± 0.2	29 ± 0.7
			381	1.91 ± 0.07	0.62 ± 0.02	8.2 ± 0.3	2.1 ± 0.3	25 ± 0.9
CNSS J0019+00	77.1	2.61 ± 0.15	573	4.26 ± 0.04	8.27 ± 0.03	11 ± 0.1	8.5 ± 0.3	21 ± 0.2
			606	3.87 ± 0.03	8.08 ± 0.04	12 ± 0.1	6.7 ± 0.2	23 ± 0.1
			731	3.12 ± 0.04	7.41 ± 0.06	14 ± 0.2	4.5 ± 0.2	22 ± 0.2
			998	1.92 ± 0.06	4.95 ± 0.09	19 ± 0.6	1.9 ± 0.2	22 ± 0.7
XMMSL1 J0740-85	75	N/A	600	1.7 ± 0.3	1.2 ± 0.3	11 ± 2.3	2.3 ± 1.8	21 ± 4.3

4.5 DISCUSSION AND CONCLUSIONS

Motivated by our previous work (Spaulding & Chang, 2021) on how the spread of energy of TDE material scales with impact parameter, β, we study the scaling of the maximum velocities of unbound debris as a function of β. We find that for a 1 $M_\odot$ main sequence star that is being tidally disrupted around a $10^6 M_\odot$ SMBH that the maximum velocities of unbound debris varies between $2 - 5 \times 10^4 \,\mathrm{km\,s^{-1}}$ and that these maximum velocities scale linearly with β. The increased maximum velocity with increasing impact parameter is in line with our previous work (Spaulding & Chang, 2021) where we showed that the spread in energy of the bound and unbound debris scale like $\beta^{1/2}$.

The high velocity unbound material interacts with the local interstellar medium and produces radio emission. We use a synchrotron emission model to determine the expected radio flux and peak frequency as a function of β for this interaction. Using this relationship, we can potentially constrain properties of the TDE and the interstellar medium in which it sits. Using radio emission data from four observed TDEs that is attributed to a nonrelativistic interaction, we use the derived relation and observed values of the peak flux and peak frequency to constrain the TDE properties such as the velocities of the unbound material and density profile of the ISM. With an assumed filling fraction $f = 0.15$, which is motivated by our simulations, we find that the TDEs: ASASSN - 14li, AT2019dsg, CNSS J0019+00 and XMMSL1 J0740-85, have velocities ($v_s \approx 2 \times 10^4 \,\mathrm{km\,s^{-1}}$) that are consistent with our simulations for $\beta \approx 2$. The final TDE considered, AT2019dsg, shows higher velocities ($v_s \approx 5 \times 10^4 \,\mathrm{km\,s^{-1}}$), which suggests a larger $\beta \sim 10$ or a more spherical outflow.

Similar to our work, Matsumoto & Piran (2021) did an in-depth equipartition analysis on data from observed TDEs to determine the velocity and solid angle required to yield the observed radio flux. They found that the radio emission from unbound debris is

much dimmer than other outflow components because of its small solid angle, $\Omega \approx 0.1$ (Yalinewich et al., 2019a). However, we find a that a larger solid angle is subtended in our simulations $\Omega = 4\pi f \approx 1.9$ for $f = 0.15$. This is in line with their constraint for $\Omega \sim 1$ for the unbound material to produce significant radio emission. In addition, they found the debris should have a distribution in which at least $\approx 10^{-2}~M_\odot$ of mass moves at $\gtrsim 2 \times 10^4$ km s^{-1}. Again this is in agreement with our simulation results and our analysis on observed radio TDEs.

Previously, Krolik et al. (2016) suggested a velocity of $\approx 11{,}000$ km s^{-1} for the unbound debris. Yalinewich et al. (2019b) did a similar analysis to ours, yielding similar results. They found the highest velocity of the ejecta to be $\gtrsim 10^4$ km s^{-1} from their simulations. By doing an equipartition analysis on data from ASASSN - 14li, they found a velocity of about 2×10^4 km s^{-1}, in line with our results in Table 4.1. However, Yalinewich et al. (2019b) assumes a $\beta = 7$ for ASASSN - 14li, while we find $\beta \approx 2$.

CHAPTER 5

Simulating TDEs with Magnetohydrodynamics

5.1 OVERVIEW

Magnetic fields are present in stars of all kinds. These magnetic fields do not greatly contribute to the energy budget of the stars themselves. However, during a TDE, the magnetic energy could be amplified by the distortion and disruption of the star. By simulating TDEs with magnetic fields, we can study the evolution of the magnetic energy to determine if the disruption of the star causes amplification in the magnetic energy. Amplification in magnetic energy can influence the observational signatures of the TDEs and large scale accretion onto the black hole.

In this section we present the first simulations of TDEs with magnetic fields using a moving mesh code. Previously, Guillochon & McCourt (2017) used FLASH, an adaptive-mesh refinement (AMR) code to study TDEs with magnetic fields. Bonnerot et al. (2017) studied this problem with a smoothed particle magnetohydrodynamics (SPHMHD). Both of these studies see amplification of the magnetic field in TDEs, but it is not clear where this amplification is happening.

5.2 METHOD

5.2.1 MHD Scheme

Our code, MANGA, (Chang et al., 2017), has had recent improvements on its implementation for an MHD solver. Prust (in-prep) has implemented several different methods for solving MHD in flux-conservative form such as Dedner et al. (2002), Tricco & Price (2012), and Powell et al. (1999). Here we will explain the moving mesh solution to solving the

MHD equations using the scheme developed by Powell et al. (1999).

Springel (2010) first point out that any flux-conservative equations of the form:

$$\frac{\partial \mathcal{U}}{\partial t} + \boldsymbol{\nabla} \cdot \boldsymbol{\mathcal{F}} = \boldsymbol{\mathcal{S}}, \tag{5.1}$$

where $\mathcal{U}$ is the state vector, $\boldsymbol{\mathcal{F}}$ is the flux, and $\boldsymbol{\mathcal{S}}$ is the source term, can be solved on a moving-mesh.

With this in mind, one can see that MHD can be implemented in a moving mesh code by setting the state vector and the flux to be:

$$\mathcal{U} = (\rho, \rho\boldsymbol{v}, \rho e, \boldsymbol{B}) \tag{5.2}$$

$$\boldsymbol{\mathcal{F}} = (\rho\boldsymbol{v}, \rho\boldsymbol{v}\boldsymbol{v} + p + \boldsymbol{B}\boldsymbol{B}, \rho e\boldsymbol{v} + p\boldsymbol{v} - \boldsymbol{B}\boldsymbol{v} \cdot \boldsymbol{B}, \boldsymbol{B}\boldsymbol{v} - \boldsymbol{v}\boldsymbol{B}), \tag{5.3}$$

ρ is the density, $\boldsymbol{v}$ is the fluid velocity, $e = \epsilon + v^2/2$ is the specific energy, ϵ is the specific internal energy and $P(\rho, \epsilon)$ is the pressure. The source term $\boldsymbol{\mathcal{S}} = (0, -\rho\boldsymbol{\nabla}\Phi, -\rho\boldsymbol{v} \cdot \boldsymbol{\nabla}\Phi)$ is unmodified, where Φ is the gravitational potential.

In addition to these equations, the magnetic field $\boldsymbol{B}$ has to fulfil the divergence constant, $\boldsymbol{\nabla} \cdot \boldsymbol{B} = 0$. Analytically, this constraint will automatically be met at all times if it is fulfilled by the initial magnetic field and evolved using Maxwell's equations. Discretization errors, however, can lead to a non-vanishing divergence of the magnetic field in numerical simulations. To remedy this, we implemented a Powell eight-wave scheme based on Powell et al. (1999) and adapted for a moving mesh as in Pakmor & Springel (2013). This scheme differs from divergence cleaning (Dedner et al., 2002) in that only an advection term is used. This advection is implemented by including additional source terms in (5.1) proportional to the divergence of the field in the momentum equation, induction equation, and energy equation:

$$\boldsymbol{\mathcal{S}}_{\mathrm{P}} = -(\boldsymbol{\nabla} \cdot \boldsymbol{B}) \begin{pmatrix} 0 \\ \boldsymbol{B} \\ \boldsymbol{v} \cdot \boldsymbol{B} \\ \boldsymbol{v} \end{pmatrix}. \tag{5.4}$$

In a finite-volume approach, such as moving-mesh, the governing equations in the form of Equation 5.1 are integrated over a cell in the grid, giving

$$\int_{cell,i} \frac{\partial \boldsymbol{\mathcal{U}}}{\partial t} dV + \int_{cell,i} \boldsymbol{\nabla} \cdot \boldsymbol{\mathcal{F}} dV = \int_{cell,i} \boldsymbol{\mathcal{S}} dV \tag{5.5}$$

$$\frac{d\boldsymbol{\mathcal{U}}}{dt} dV + \oint_{\partial cell,i} \boldsymbol{\mathcal{F}} \cdot \hat{\boldsymbol{n}} dS = \boldsymbol{\mathcal{S}}_i V_i \tag{5.6}$$

where $\boldsymbol{\mathcal{U}}_i$ and $\boldsymbol{\mathcal{S}}_i$ are the cell-averaged conserved variables and source terms, respectfully. In order to evaluate the integral, we must put it in discrete form:

$$\frac{d\boldsymbol{\mathcal{U}}}{dt} V_i + \sum_{faces} \boldsymbol{\mathcal{F}} \cdot \hat{\boldsymbol{n}} dS = \boldsymbol{\mathcal{S}}_i V_i \tag{5.7}$$

where the $\boldsymbol{\mathcal{F}} \cdot \hat{\boldsymbol{n}}$ terms are evaluated at the midpoints of the faces of the cell. The source term $\boldsymbol{\mathcal{S}}_i$ is proportional to the volume average of $\boldsymbol{\nabla} \cdot \boldsymbol{B}$ for a cell.

We apply the divergence source terms for all active cells at the same time when we calculate and apply the local fluxes. In each time-step, we first define the magnetic field

perpendicular to a cell interface, $B_x = \frac{1}{2}(B_{x,L} + B_{x,R})$ where x is the face normal. This value of B_x is then used in the Riemann solver. The average divergence of the magnetic field is then

$$\boldsymbol{\nabla} \cdot \boldsymbol{B}_{cell,i} = \frac{1}{V_i} \sum_{faces} \boldsymbol{B} \cdot \hat{\boldsymbol{n}} dS \tag{5.8}$$

The equation to be integrated in time is therefore:

$$\frac{d\boldsymbol{\mathcal{U}}}{dt} V_i + \sum_{faces} \boldsymbol{\mathcal{F}} \cdot \hat{\boldsymbol{n}} dS = - \begin{pmatrix} 0 \\ \boldsymbol{B} \\ \boldsymbol{v} \cdot \boldsymbol{B} \\ \boldsymbol{v} \end{pmatrix}_i \boldsymbol{B} \cdot \hat{\boldsymbol{n}} dS \tag{5.9}$$

These source terms encode a passive advection of $\boldsymbol{\nabla} \cdot \boldsymbol{B}/\rho$ with the flow and counteract further growth of local $\boldsymbol{\nabla} \cdot \boldsymbol{B}$ errors. This scheme is the most efficient for TDEs because the time step is determined locally, which offers a substantial increase in performance. On the other hand, the scheme proposed by Dedner et al. (2002) is restricted by a maximum signal speed, c_h defined by the largest signal speed present in the simulation at a given time (Pakmor et al., 2011).

5.2.2 Initial Conditions

We used the moving-mesh simulation code, MANGA (Chang et al., 2017; Prust & Chang, 2019), to conduct a parameter study of a 1 $M_\odot$ star encountering a $10^6 M_\odot$ SMBH with a penetration depth, β = 2. We also varied the initial magnetic field on the surface of the

star with values of 1, 10, and 100 Gauss to see the influence of the initial field. We used between $10^5(6.9 \times 10^5)$ and $4 \times 10^5(2.7 \times 10^6)$ mesh-generating points for the star (star and background). We model the SMBH as a dark matter particle with a softened gravitational length of 6.14×10^{11} cm. The interested reader is referred to Spaulding & Chang (2021) for more details.

5.3   RESULTS

5.3.1   Outflow

We find a significant amount of mass flowing outward radially from the SMBH in our MHD simulations, shown in Figure 5.1. This is not a result that we found in our HD simulations. To look closer at this outflow, we restricted our data to the $z < 0$ plane, where the outflow was present but the tidal tail is not. We looked at this outflow for early times only, just after disruption, because of numerical time limitations. The outflow appears more prevalent about 15 hours after disruption. The data from our simulations is taken at a distance of $8r_T$ from the SMBH.

The outflow is found to have a cumulative mass of $\sim 0.01 \, M_\odot$ shown in Figure 5.2 for early times. We also find velocities of the outflow material on the order of $\sim 10^4$. We take the average velocity of 10^9 cm from our simulations to model our photosphere in Section 5.3.2.

Finally, we looked at the mass flux of the outflow material as a function of time, shown in Figure 5.3. The mass flux remains relatively constant from 15 hours after disruption through the next 20 hours. The mass flux rate of the outflow material is found to be the same as the accretion rate of the bound material at early times, indicating that the outflow is a consequence of the accretion. Following this, we looked at the accretion rate at early times before it hits its peak to model the mass flux rate of the outflow similarly.

5.3.2 Photosphere

We find that thee outflow is sufficiently dense to reprocess emission, therefore we now use our results from 5.3.1 to calculate parameters of a photosphere created from the outflow. We define the radius of the photosphere as the distance where the optical depth (τ) = 1.

If we take our peak outflow mass flux rate to be equal to the peak accretion rate, $\dot{M}_{out} \approx \dot{M}_{acc}$, we get

$$\dot{M}_{out} \approx 1 M_\odot/\text{year} \approx 6 \times 10^{25} g/s \tag{5.10}$$

Using the result we found in Figure 5.3 of a constant rate and a spherical outflow, the mass flux rate is

$$\dot{M}_{out} = 4\pi r^2 \rho v = \text{constant} \tag{5.11}$$

We define the scattering photosphere as

$$\tau(r_{ph}) = \int_{r=\infty}^{r_{ph}} \kappa\rho(r)dr = \int_{r=\infty}^{r_{ph}} \kappa\frac{\dot{M}}{4\pi r^2 v} = \kappa\frac{\dot{M}}{4\pi r_{ph} v} = 1 \tag{5.12}$$

In Figure 5.5 we plot the accretion rate of the bound material at early times before it peaks. We find a linear relationship between accretion rate and time, and we use this result to model the resulting photosphere in Section 5.3.2. With the connection of the inflowing material with the outflowing material, this suggests that the photosphere from the outflow would also be expanding linearly in time.

From our simulations we know that $\dot{M} \propto t$, giving us the result of r_{ph} expanding linearly in time. Using our values for $\dot{M}_{out}$ from Equation 5.10 and velocity from 5.3.1, we find

$$r_{ph}(t) = 2 \times 10^{15} \left(\frac{\dot{M}(t)}{1 M_\odot/\text{year}} \right) \left(\frac{v}{10^9 \text{cm/s}} \right)^{-1} \tag{5.13}$$

5.3.3 Connecting to Observations

TDEs have been observed with a wide variation of blackbody radii, as shown in Figure 5.6. In her review, Gezari (2021) plotted the blackbody radius for TDEs observed in optical and X-ray. The difference in radii is several orders of magnitude. Our results show a photospheric radius consistent with the optically selected TDES in Figure 5.6 of $2 \times 10^{15} cm$. This radius depends on the velocity of the outflow, v, and the mass flux rate, $\dot{M}$. The outflow model we present of reprocessing radiation that appears as blackbody radiation results in the blackbody radius that is seen in optical observational data from TDEs, as shown in Figure 5.6.

Outflows have been modeled as the source of optical TDE emission in several TDEs. Hung et al. (2019b) suggested that the optical signatures of the TDE AT2018zr were indicative of a spherical outflow. They calculated a photosphere radius r_{ph} of 10^{15} cm that was responsible for the emission of the observed continuum flux at wavelengths near Hα. The gas density falls off as r^{-2} at radii beyond r_{ph} out to a maximum radius r_{out}, where the velocity is v_{max}. They found a maximum radius of 3×10^{15} and a maximum velocity of $1.75 \times 10^4 \text{km s}^{-1}$. Figure 5.7 shows the optical observations fit to a spherical outflow model. The observed maximum radius of the outflow from this TDE of 3×10^{15} cm matches the photosphere radius in our simulations.

As mentioned in Section 4.4, by constructing the bolometric light curve of AT2019qiz, Nicholl et al. (2020) fit a blackbody function to estimate the temperature, radius, and missing energy outside of the observed wavelength range. Most significantly to this work, the result was that the blackbody radius grows linearly up to maximum light. Assuming spherical symmetry, Nicholl et al. (2020) used a blackbody function to compute the photospheric radius at different epochs. With this data, the velocity of the outflow can be computed, which was found to be 2200 km/s for this TDE. This again is similar to the magneto-centrifugal driven outflow model we propose from our simulations.

Holoien et al. (2019) describe discovery and the early evolution of the TDE ASASSN-19bt. This is a TDE discovered by the All-Sky Automated Survey for Supernovae (ASAS-SN) in the optical/UV band with follow-up from Swift and XMM-Newton. Ground data from 32 days before peak through 37 days after peak allows Holoien et al. (2019) to look closely at the evolution of the photosphere radius prior to peak light. From Swift fits to a blackbody, the radius of the photosphere increases about an order of magnitude from 30 days prior to peak light to the time of peak light. They found that the apparent photosphere is expanding very slowly compared to the local escaped speed with a velocity between 3000-4000 km/s. It is not obvious to them where this velocity comes from, but we would argue that it is the result of an outflow from the TDE and the growing accretion rate and hence the outflow rate.

5.4   DISCUSSION AND CONCLUSIONS

We have implemented an MHD solver to MANGA based on the Powell eight wave scheme, and have used it to study the effect of magnetic fields on TDEs. Though magnetic fields do not contribute much to the energy budget of the star itself, we find that the presence of an initial magnetic field on the surface of the star contributes greatly to the
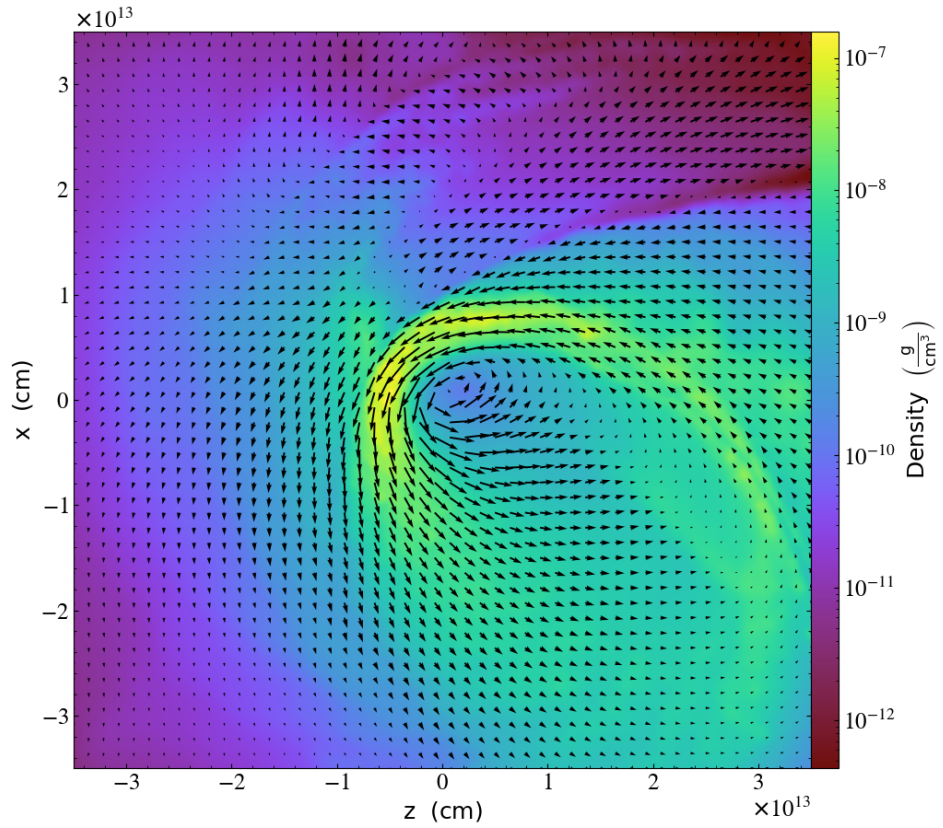
Figure 5.1: The density projection for a $1 M_\odot$ star with an initial magnetic field strength of 1 G disrupted by a $10^6 M_\odot$ SMBH. This snapshot is taken about 1 day after disruption. Velocity vectors show an outflow moving away from the SMBH with significant velocity.
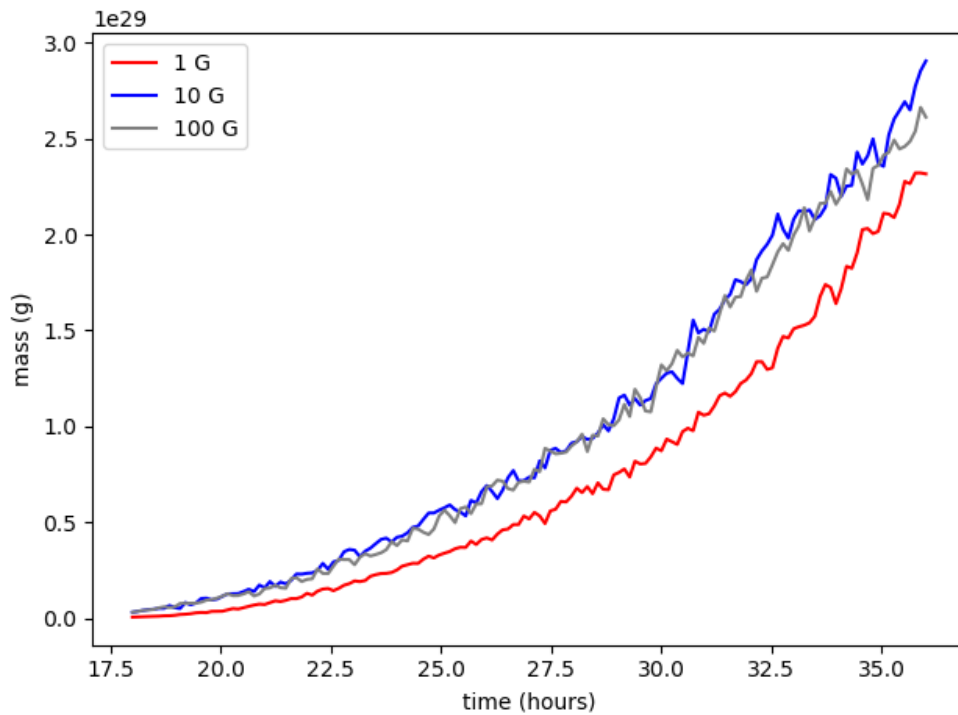
Figure 5.2: The cumulative mass of the outflow is shown over time for stars with initial magnetic fields of 1, 10 and 100 Gauss. Our results show small variation in mass, possibly due to accumulation as the outflow expands outwards.
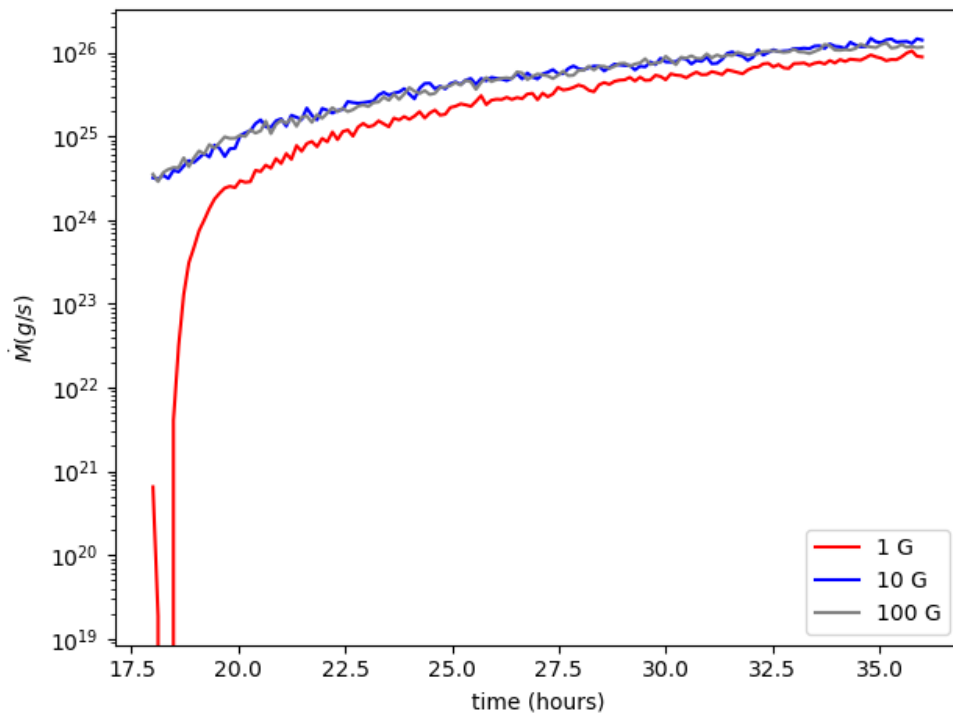
Figure 5.3: The mass flux rate of the outflow is shown over time for stars with initial magnetic fields of 1, 10 and 100 Gauss. Our results show small variation in $\dot{M}$, supporting a constant expansion rate for the outflow material.
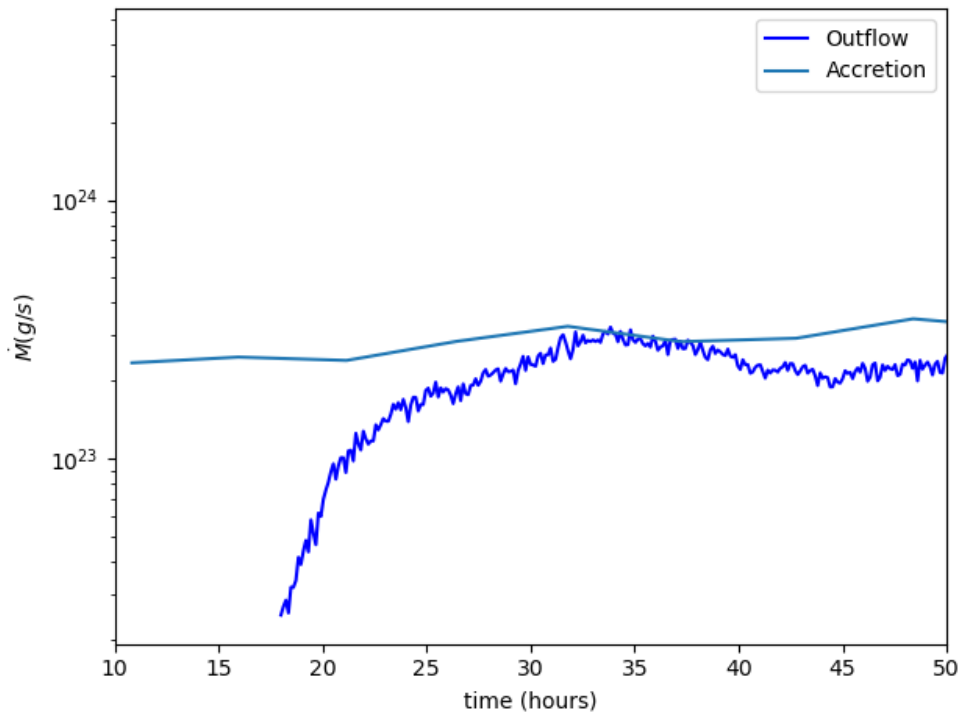
Figure 5.4: The mass flux rate of the outflow and the accretion rate of the bound material is shown over time for stars with an initial magnetic fields of 10 Gauss. We offset the accretion rate by 40 days to compare the values. By doing this, we see the variables approach the same value, indicating a connection between the outflow mass flux and the accretion rate.
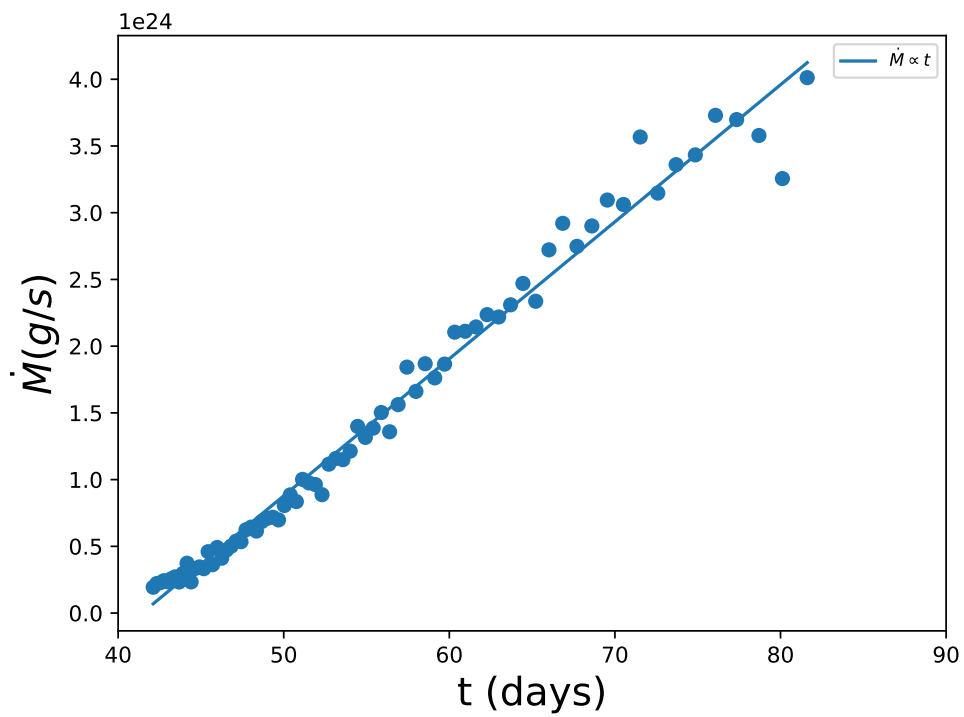
Figure 5.5: The fallback rate of the material is shown at early times for a $1M_\odot$ star with an initial magnetic field of 1 G. The fallback rate increases linearly with time.
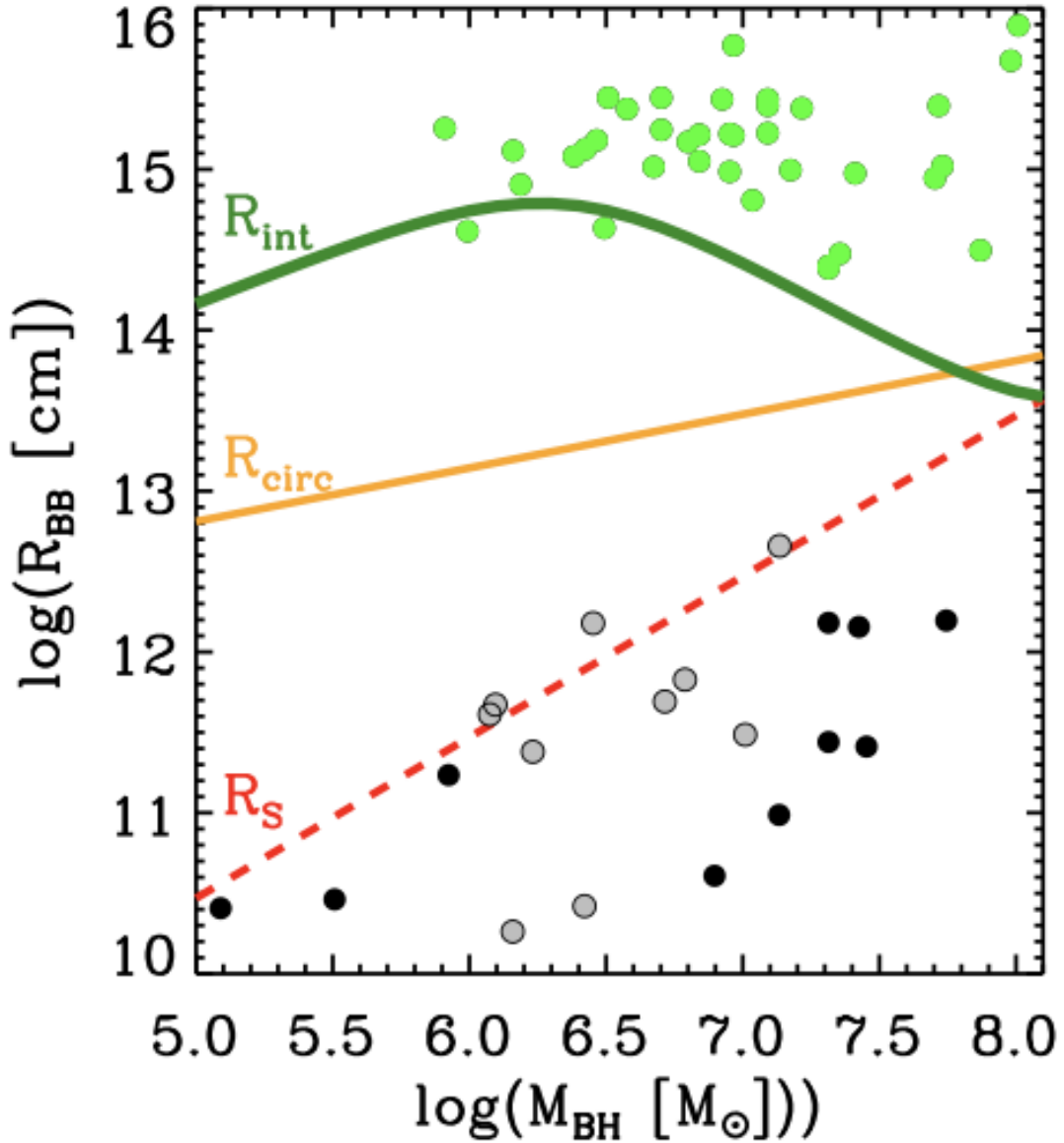
Figure 5.6: Blackbody radius as a function of black hole mass estimated from the total galaxy mass for UV/optical selected TDEs (green), X-ray selected TDEs (black), and the soft X-ray component of UV/optically selected TDEs (grey). While the radius of the soft X-ray component appears to track the increase of the Schwarzschild radius linearly, with mass, $R_S \propto M_{\rm BH}$ (plotted with a red dashed line) the UV/optical component appears not to have a strong dependence on black hole mass and is a factor of 100 larger than the expected size of the circularized debris disk, $R_{circ} \sim 2R_T$ (plotted in yellow). Reprinted from Gezari (2021).
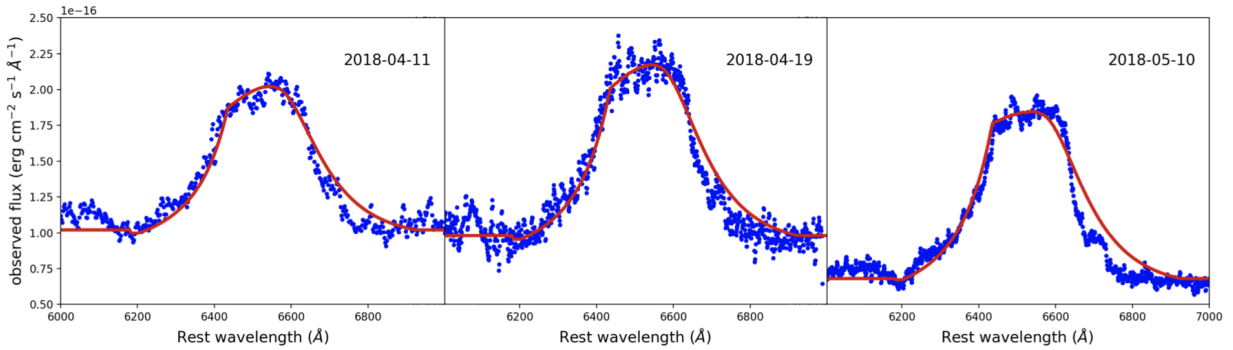
Figure 5.7: Hα line profiles, with fits to a spherical outflow model for the broad emission. Reprinted from Hung et al. (2019b).

outflowing material from a TDE. The outflow of mass we find is only present in simulations with an initial magnetic field, but does not seem to depend on the size of the initial magnetic field itself.

We find an outflow expanding linearly with time that could explain optical signatures of a TDE, such as the varying ratios of optical to X-ray emission that have been observed. We also find that the outflow rate is correlated with the inflow rate. By expanding out to peak inflow rate, we can compute a photosphere with a size that is consistent with optical TDEs. Lastly, we find that the inflow rate scales linearly with time for early times, which suggests the photosphere also expands linearly out to the peak radius.

TDEs such as AT2018zr, AT2019qiz, and ASASSN-19bt have been modeled to have evolving photospheres with increasing radii. We suggest that an outflow from the TDE provides the mechanism for reprocessing of the X-ray emission due to accretion into optical emission. With this model, we find a photosphere radius of $\sim 2 \times 10^{15}$ cm, which is in line with blackbody radii that have been observed in a number of optically selected TDEs. This indicates that the optical emission from a TDE could be a direct result of the accretion onto the SMBH. With this in mind, simulating the accretion disk on long timescales could give us a better understanding of the outflow material as well.
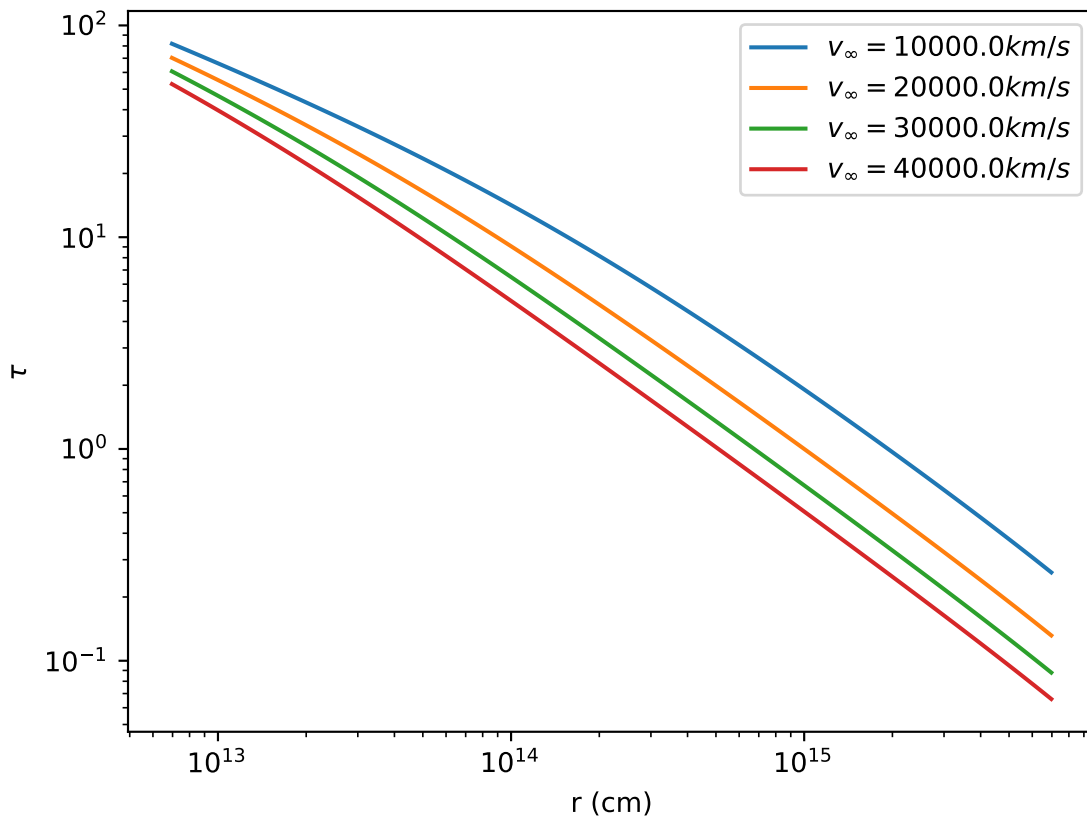
Figure 5.8: The optical depth of the photosphere is shown for varying radii and velocities. The optical depth does not exceed 100, showing the photosphere is moderately thick. At $\tau = 1$ we recover the photosphere radius we calculated.
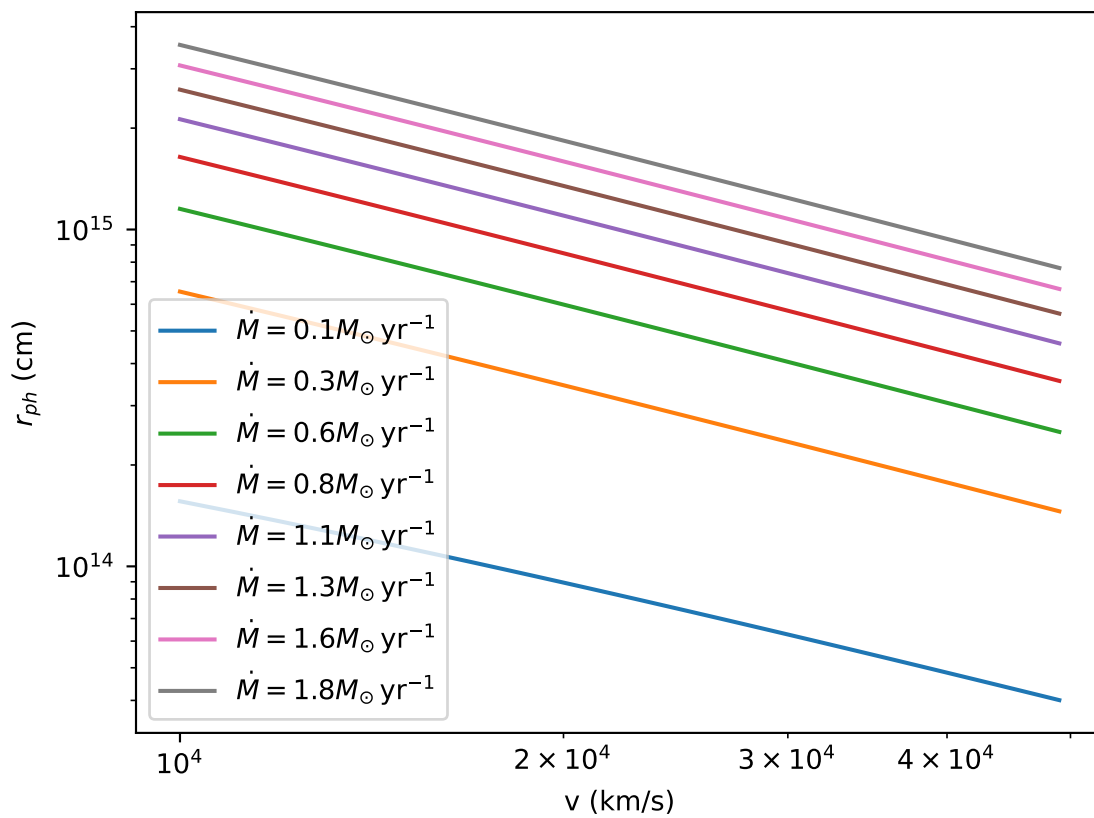
Figure 5.9: The photosphere radius is shown for varying velocities and $\dot{M}$ values. The radius remains between 10^{14} and 10^{16} cm, matching optical observations.

CHAPTER 6

Conclusion

Tidal disruption events are critical tools in detecting and understanding supermassive black holes, especially in quiescent galaxies. Other detection methods depend on active emission from the accretion disk, or merging of black holes in the case of gravitational waves. TDEs offer an avenue to observe SMBHs on observational timescales, accretion physics across a range of rates on short timescales, and give us emission from a range of wavelengths. Using observations from the different spectra, we can gain a more complete picture of the event and the black hole itself. By conducting a parameter study of TDEs using simulations, we can better understand the information we can gain from specific observations. In Chapter 3, I discussed a parameter study of impact parameter, β, on TDEs and the resulting energy spread in the debris. With this, we were able to show the effect impact parameter has on the time of peak luminosity and the evolution of the accretion rate. By being able to infer the impact parameter of a TDE, we are able to probe the dynamics near the centers of galaxies. For example, the distribution of β can place constraints on the mass distribution in galactic centers, and the general orbits of stars in the central regions. In the future, this parameter study can be applied to a greater range in impact parameter, specially low β to see how partial disruption affects peak luminosity and the accretion rate.

TDEs have been observed in the X-ray, radio, optical and uv wavelengths, and while the X-ray emission is accepted to be powered by accretion, the mechanisms that power the radio and optical emission are still not completely understood. In Chapter 4, we model the radio emission as synchrotron emission from the unbound debris. We use velocities and mass distributions from our simulations to create the synchrotron model that closely

aligns with TDE radio observations. Similar to Chapter 3, we find a relationship between impact parameter and radio emission flux. This gives us another method to infer impact parameter of a TDE and be able to better describe the distribution of the center of the galaxy it is in. With radio TDE observational data, we were also able to use our model to determine the density profile of the surrounding medium and the expected velocity of the unbound debris. Radio observations are a crucial tool in interpreting characteristics of TDEs because the emission can be detected with ground based telescopes. By modeling TDE radio emission as synchrotron emission, we gain information about the surrounding environment and velocity of the material generating the emission. This adds to our knowledge about galactic centers and their mass distribution.

By adding magnetohydrodynamics to our simulations, we observed an outflow that was not present in the purely hydrodynamic simulations. The outflow rate scales with the accretion rate, indicating a connection between the two and a model for the outflowing material. With this result, we can model the expected photosphere from the outflow, and we show that the velocity of the outflow and the radius of the photosphere are consistent with optical observations of TDEs. Therefore, we would argue that the optical emission is due to reprocessing of the emission from the accretion disk. This argument is supported by our calculations of the optical thickness showing the photosphere is moderately optically thick, having a value of less than 100 for all of our $\dot{M}$ and velocity values. This makes these simulations a great candidate for inclusion of radiation hydrodynamics. This project is one that could be easily expanded upon by running for longer times and looking at the dynamics of the outflows. Outflows are also a proposed mechanism for the radio emission from TDEs, and this is something that could be modeled from our simulations in the future.

The addition of magnetohydrodynamics in our simulations opens up possibilities for

many studies in the future. One future opportunity is looking at the evolution of the accretion disk on long timescales and the effect of the magnetic field. Because MHD is a new addition to our code, a parameter study on different initial magnetic field strengths and the effects this has on outflow velocity, mass, evolution is another option for a future study.

TDEs are an essential tool in understanding several areas of physics such as black hole dynamics, accretion, radiation, jets and more. By studying these through hydrodynamic simulations, we can gain the most information possible from observational data. As our observational technology improves, such as the LSST telescope, detections of TDEs will exponentially increase, making this a crucial time to gain a better understanding of the different physical processes present for a TDE. A complete picture of these events will get us closer to understanding the SMBHs at the centers of galaxies, the mass distributions of the centers of galaxies, and the evolution the accretion disks that surround the SMBH.

BIBLIOGRAPHY

Agertz O., et al., 2007, , 380, 963

Alexander K. D., Berger E., Guillochon J., Zauderer B. A., Williams P. K. G., 2016, , 819, L25

Alexander K. D., Wieringa M. H., Berger E., Saxton R. D., Komossa S., 2017, , 837, 153

Alexander K. D., van Velzen S., Horesh A., Zauderer B. A., 2020, , 216, 81

Anderson M. M., et al., 2020, , 903, 116

Auchettl K., Guillochon J., Ramirez-Ruiz E., 2017, , 838, 149

Barniol Duran R., Nakar E., Piran T., 2013, , 772, 78

Bellm E. C., et al., 2019, , 131, 018002

Berger E., Zauderer A., Pooley G. G., Soderberg A. M., Sari R., Brunthaler A., Bietenholz M. F., 2012, , 748, 36

Bonnerot C., Price D. J., Lodato G., Rossi E. M., 2017, , 469, 4879

Bricman K., Gomboc A., 2020, , 890, 73

Cendes Y., Alexander K. D., Berger E., Eftekhari T., Williams P. K. G., Chornock R., 2021, , 919, 127

Chambers K. C., et al., 2016, arXiv e-prints, p. arXiv:1612.05560

Chang P., Etienne Z., 2020, arXiv e-prints, p. arXiv:2002.09613

Chang P., Wadsley J., Quinn T. R., 2017, , 471, 3577

Chang P., Davis S. W., Jiang Y.-F., 2020, , 493, 5397

Chevalier R. A., 1998, , 499, 810

Dai L., McKinney J. C., Roth N., Ramirez-Ruiz E., Miller M. C., 2018, , 859, L20

Dedner A., Kemm F., Kröner D., Munz C. D., Schnitzer T., Wesenberg M., 2002, Journal of Computational Physics, 175, 645

Dolag K., Vazza F., Brunetti G., Tormen G., 2005, , 364, 753

Duffell P. C., 2016, , 226, 2

Duffell P. C., MacFadyen A. I., 2011, , 197, 15

Esquej P., Saxton R. D., Freyberg M. J., Read A. M., Altieri B., Sanchez-Portal M., Hasinger G., 2007, , 462, L49

Ferrarese L., Ford H., 2005, , 116, 523

Fryxell B., et al., 2000, , 131, 273

Gaburov E., Johansen A., Levin Y., 2012, , 758, 103

Gafton E., Rosswog S., 2019, , 487, 4790

Gebhardt K., Adams J., Richstone D., Lauer T. R., Faber S. M., Gültekin K., Murphy J., Tremaine S., 2011, , 729, 119

Genzel R., Eisenhauer F., Gillessen S., 2010, Reviews of Modern Physics, 82, 3121

Gezari S., 2021, Annual Review of Astronomy and Astrophysics, 59, 21

Ghez A. M., Salim S., Hornstein S. D., Tanner A., Lu J. R., Morris M., Becklin E. E., Duchene G., 2005, The Astrophysical Journal, 620, 744

Gingold R. A., Monaghan J. J., 1977, , 181, 375

Gnedin N. Y., 1995, , 97, 231

Goicovic F. G., Springel V., Ohlmann S. T., Pakmor R., 2019, , 487, 981

Guillochon J., McCourt M., 2017, , 834, L19

Guillochon J., Ramirez-Ruiz E., 2013, , 767, 25

Guillochon J., Ramirez-Ruiz E., 2015, , 809, 166

Guillochon J., Ramirez-Ruiz E., Rosswog S., Kasen D., 2009, , 705, 844

Hinkle J. T., Holoien T. W. S., Shappee B. J., Auchettl K., Kochanek C. S., Stanek K. Z., Payne A. V., Thompson T. A., 2020, , 894, L10

Holoien T. W. S., et al., 2019, , 883, 111

Holoien T. W. S., et al., 2020, arXiv e-prints, p. arXiv:2003.13693

Hopkins P. F., 2015, , 450, 53

Hung T., et al., 2018, , 238, 15

Hung T., et al., 2019a, , 879, 119

Hung T., et al., 2019b, The Astrophysical Journal, 879, 119

Jetley P., Gioachin F., Mendes C., Kale L. V., Quinn T. R., 2008, Proceedings of IEEE International Parallel and Distributed Processing Symposium

Jetley P., Wesolowski F., Gioachin F., Kale L. V., Quinn T. R., 2010, Proceedings of the 2010 ACM/IEEE International Conference for High Performance Computin

Jiang Y.-F., Guillochon J., Loeb A., 2016, , 830, 125

Jiang Y.-F., Stone J. M., Davis S. W., 2019, , 880, 67

Kormendy J., Fisher D. B., Cornell M. E., Bender R., 2009, , 182, 216

Krolik J., Piran T., Svirski G., Cheng R. M., 2016, , 827, 127

Lattanzio J., 1986, in Bulletin of the American Astronomical Society. p. 963

Law N. M., et al., 2009, , 121, 1395

Li D., et al., 2020, , 891, 121

Lin D., Carrasco E. R., Grupe D., Webb N. A., Barret D., Farrell S. A., 2011, , 738, 52

Lu W., Bonnerot C., 2020, , 492, 686

Lucy L. B., 1977, , 82, 1013

Maguire K., Eracleous M., Jonker P. G., MacLeod M., Rosswog S., 2020, , 216, 39

Mainetti D., Lupi A., Campana S., Colpi M., Coughlin E. R., Guillochon J., Ramirez-Ruiz E., 2017, , 600, A124

Martin D. C., et al., 2005, , 619, L1

Matsumoto T., Piran T., 2021, , 507, 4196

Matsumoto T., Piran T., Krolik J. H., 2022, , 511, 5085

Matthias M.-F., Mark P., Markus G., Richard K., Martin W., 2007, in GROSS M., PFISTER H., eds, The Morgan Kaufmann Series in Computer Graphics, Point-Based Graphics. Morgan Kaufmann, Burlington, pp 340–387, doi:https://doi.org/10.1016/B978-012370604-1/50008-0, https://www.sciencedirect.com/science/article/pii/B9780123706041500080

Menon H., Wesolowski L., Zheng G., Jetley P., Kale L., Quinn T., Governato F., 2015, Computational Astrophysics and Cosmology, 2, 1

Miller M. C., 2015, , 805, 83

Mummery A., Balbus S., 2020, arXiv e-prints, p. arXiv:2006.00803

Nicholl M., Short P., Lawrence A., Ross N., Smartt S., 2019, Transient Name Server As-
troNote, 59, 1

Nicholl M., et al., 2020, , 499, 482

Pacholczyk A. G., 1970, Radio astrophysics. Nonthermal processes in galactic and extra-
galactic sources

Pakmor R., Springel V., 2013, , 432, 176

Pakmor R., Bauer A., Springel V., 2011, , 418, 1392

Paxton B., Bildsten L., Dotter A., Herwig F., Lesaffre P., Timmes F., 2011, , 192, 3

Paxton B., et al., 2013, , 208, 4

Paxton B., et al., 2015, , 220, 15

Pearce F. R., Couchman H. M. P., 1997, , 2, 411

Pen U.-L., 1998, , 115, 19

Phinney E. S., 1989, in Morris M., ed., IAU Symposium Vol. 136, The Center of the Galaxy.
p. 543

Piran T., Svirski G., Krolik J., Cheng R. M., Shiokawa H., 2015, , 806, 164

Piro A. L., Lu W., 2020, , 894, 2

Powell K. G., Roe P. L., Linde T. J., Gombosi T. I., De Zeeuw D. L., 1999, Journal of Com-
putational Physics, 154, 284

Prust L. J., Chang P., 2019, , 486, 5809

Quataert E., 2004, , 613, 322

Rees M. J., 1988, , 333, 523

Rosswog S., 2007, Astronomische Nachrichten, 328, 663

Roth N., Kasen D., 2018, , 855, 54

Ryu T., Krolik J., Piran T., Noble S. C., 2020, arXiv e-prints, p. arXiv:2001.03502

Sargent W. L. W., Young P. J., Boksenberg A., Shortridge K., Lynds C. R., Hartwick F. D. A., 1978, , 221, 731

Saxton R. D., Read A. M., Esquej P., Komossa S., Dougherty S., Rodriguez-Pascual P., Barrado D., 2012, , 541, A106

Saxton R., Komossa S., Auchettl K., Jonker P. G., 2020, , 216, 85

Shappee B. J., et al., 2014, , 788, 48

Shiokawa H., Krolik J. H., Cheng R. M., Piran T., Noble S. C., 2015, , 804, 85

Spaulding A., Chang P., 2021, , 501, 1748

Springel V., 2005, , 364, 1105

Springel V., 2010, , 401, 791

Springel V., Yoshida N., White S. D. M., 2001, , 6, 79

Stadel J. G., 2001, PhD thesis, UNIVERSITY OF WASHINGTON

Stein R., et al., 2021, Nature Astronomy, 5, 510–518

Steinberg E., Yalinewich A., Sari R., 2016, , 459, 1596

Steinberg E., Coughlin E. R., Stone N. C., Metzger B. D., 2019, , 485, L146

Stone N. C., Metzger B. D., 2016, , 455, 859

Stone J. M., Gardiner T. A., Teuben P., Hawley J. F., Simon J. B., 2008, , 178, 137

Stone N., Sari R., Loeb A., 2013, , 435, 1809

Stone N. C., Kesden M., Cheng R. M., van Velzen S., 2019, General Relativity and Gravitation, 51, 30

Stone N. C., Vasiliev E., Kesden M., Rossi E. M., Perets H. B., Amaro-Seoane P., 2020, , 216, 35

Teyssier R., 2002, , 385, 337

Tonry J. L., et al., 2018, , 130, 064505

Toro E., 2009, Riemann Solvers and Numerical Methods for Fluid Dynamics: A Practical Introduction. Springer Berlin Heidelberg

Toro E. F., Spruce M., Speares W., 1994, Shock Waves, 4, 25

Tricco T. S., Price D. J., 2012, Journal of Computational Physics, 231, 7214

Turk M. J., Smith B. D., Oishi J. S., Skory S., Skillman S. W., Abel T., Norman M. L., 2011, The Astrophysical Journal Supplement Series, 192, 9

Ulmer A., 1999, , 514, 180

Virtanen P., et al., 2020, Nature Methods, 17, 261

Weissbein A., Sari R., 2017, , 468, 1760

Whitehurst R., 1995, , 277, 655

Wyrzykowski Ł., et al., 2014, , 64, 197

Yalinewich A., Steinberg E., Sari R., 2015, , 216, 35

Yalinewich A., Guillochon J., Sari R., Loeb A., 2019a, , 482, 2872

Yalinewich A., Steinberg E., Piran T., Krolik J. H., 2019b, , 487, 4083

York D. G., et al., 2000, , 120, 1579

Zauderer B. A., et al., 2011, , 476, 425

Zauderer B. A., Berger E., Margutti R., Pooley G. G., Sari R., Soderberg A. M., Brunthaler A., Bietenholz M. F., 2013, , 767, 152

van Velzen S., et al., 2011, , 741, 73

van Velzen S., et al., 2016, Science, 351, 62

van Velzen S., Holoien T. W. S., Onori F., Hung T., Arcavi I., 2020, , 216, 124

Alexandra E. Spaulding

Milwaukee, WI 53202
(920) 917-9734
spauld23@uwm.edu

EDUCATION

PhD, Physics   September 2018 - Present
University of Wisconsin – Milwaukee, Milwaukee, WI
- Researching as part of the Center for Gravity, Cosmology and Astrophysics group
- Performing the role of Teaching Assistant for intermediate and advanced level physics courses

Bachelor of Science, Physics   September 2014 – May 2018
Loyola University Chicago, Chicago, IL
- Major in Physics with a Minor in Mathematics
- 3.62/4.00 cumulative GPA, cum laude
- Dean's List for 7 consecutive semesters

Semester Abroad   August - December 2016
St Louis University, Madrid, Spain
- Became proficient in Spanish while studying abroad and living with a Spanish family

TEACHING EXPERIENCE

Undergraduate Teacher Assistant   September 2018 - Present
University of Wisconsin – Milwaukee, Milwaukee, WI
- Leading discussion classes for Introduction to Physics course
- Led a lab section by discussing physics concepts and showing how to implement the lab
- Given the role as a tutor in the University library for any level physics student to ask for help

Introductory Physics Teacher Assistant   January – May 2017
Loyola University Chicago, Chicago, IL
- Facilitated group work in an Introduction to Physics course
- Answered any questions form students
- Explained physics concepts and provided examples using various approaches
- Provided feedback to the professor on the development of the students' understanding

RESEARCH EXPERIENCE

Research Assistant   October 2018 – Present
University of Wisconsin – Milwaukee, Milwaukee, WI
- Tasks include running and analyzing cosmological simulations, specifically tidal disruption events, programming the simulations using Python, and interpreting the results of the simulations

Research Assistant   August 2017 – May 2018

Northwestern University, Evanston, IL
- Assist lab managers and postdoctoral candidates to create high school level physics lesson plans incorporating block based coding connected to an Arduino robot
- Worked with high school students to determine the best way to improve coding techniques and physics concept understanding with the new lab lesson plans such as a light sensor lab, motion lab and a gas sensor lab

Research Assistant (REU)   May – August 2017

Southern Illinois University Carbondale, Carbondale, IL
- Collaborated on a quantum nonlocality physics research project with an associate physics professor by creating node diagrams, matrices, and probability diagrams to find the solution to Mermin's game that resulted in co-authoring a publication submitted in the *Physical Review A*
- Discussed progress and future explorations with a graduate student to determine what the finding of a solution in Mermin's game meant for the future of quantum information processing
- Presented a poster of the research findings at an REU symposium
- Presented a slide show of my research to the Loyola Chicago Physics Department

Research Assistant   January – May 2015

Loyola University Chicago, Chicago, IL
- Conducted research on how to improve the Atwood machine with three other students and used motion sensors to compare the accuracy of the original Atwood machine with our modernized version

PUBLICATIONS

Alexandra Spaulding, Philip Chang, "Radio emission from simulated tidal disruption events", *Monthly Notices of the Royal Astronomical Society*, Volume 515, Issue 2, September 2022, Pages 1699–1704.

Alexandra Spaulding, Philip Chang, "The effect of impact parameter on tidal disruption events", *Monthly Notices of the Royal Astronomical Society*, Volume 501, Issue 2, February 2021, Pages 1748–1754.

AWARDS

FINESST Fellowship (NASA)   September 2021 – May 2023

NASA Wisconsin Space Grant Consortium Award   Summers 2020, 2021, 2022

Nicholas J. Papastamatiou Scholarship   Spring 2022

UW-Milwaukee Research Excellence Award   2018 - 2022

Chancellor's Graduate Student Award   2018 - 2022